



TECHNICAL ARTICLE

Effects of Heat Treatment on the Mechanical Properties of Fe-Based ER70S-6 Cladding on Aluminum Substrate Using Cold Metal Transfer Process

Bappa Das, Biranchi N. Panda, and Uday S. Dixit

Submitted: 19 November 2022 / Revised: 29 January 2023 / Accepted: 4 February 2023

This work highlights the impact of post-heat treatment on the mechanical properties of Fe-based ER70S-6 cladding on AA 6061-T6 substrate using cold metal transfer method. The post-heat treatment used on the extracted samples was of four types—(1) sample heating up to 600 °C followed by a 1-h holding and furnace cooling for 24 h, (2) sample heating up to 600 °C followed by a 1-h holding and water quenching, (3) artificial age hardening by heating the sample up to 175 °C, holding it for 24 h and then furnace cooling for 6 h and (4) deep cryo-treatment by dipping the sample in liquid nitrogen (-196°C) for 1 h and then bringing to ambient temperature. The effects of heat treatment on the grain size, microstructure and surface roughness were analyzed by optical microscopy, field emission scanning electron microscopy and atomic force microscopy, respectively. The average grain size of the cladded layer was 27 μm , which increased to 30 μm in Type 1 heat treatment and 29 μm in Type 3 heat treatment. However, in Type 2 and Type 4 heat treatment, the average grain size reduced to 24 and 20 μm , respectively; this resulted in the reduction of mean surface roughness from 46 to 41 nm and 25 nm in Type 2 and Type 4, respectively, when evaluated at a surface area of 100 $(\mu\text{m})^2$. In Type 1 and Type 3 of heat treatment, the mean surface roughness increased. Type 4 heat treatment provided dense martensitic phase and enhanced dislocation density ($10.78 \times 10^{16}/\text{m}^2$ as against $6.08 \times 10^{16}/\text{m}^2$ in the as-cladded layer). The grain refinement, dense martensitic phase and enhanced dislocation density increased hardness, wear resistance and tensile strength in Type 4 heat treatment, which emerged as the best heat treatment for enhancement of hardness and wear resistance.

Keywords aluminum alloy, cladding, cold metal transfer, hardness, heat treatment, wear

1. Introduction

Developed by Fronius company of Austria in 2004, cold metal transfer (CMT) is a modified gas metal arc welding (GMAW) process that uses a short-circuit transfer mechanism to deposit the material with better weld bead aesthetics, controlled droplet detachment and low heat input (Ref 1). The amount of heat delivered to the weld bead is low in the CMT process resulting in reduced distortion. The process also has high production rate due to the controlled fast electrode motion. Because the wire is retracted mechanically during the short-circuit period, CMT process is also known as mechanically assisted droplet deposition process. As a robotic arm carries out the wire, it is easy to carry out deposition on a complex route. The heat input used for melting of wire depends on different process parameters like voltage, current, wire feed speed and stand-off distance (Ref 1).

Bappa Das, Biranchi N. Panda, and Uday S. Dixit, Department of Mechanical Engineering, Indian Institute of Technology Guwahati, Guwahati, Assam 781 039, India. Contact e-mails: uday@iitg.ac.in and usd1008@yahoo.com.

The CMT can be used for depositing the material on the substrate to enhance the targeted microstructural and mechanical properties, which is called cladding process. Both heat input during deposition and heat transfer after deposition affect the properties of the cladded or coated material (Ref 1). The greatest distinguishing feature of CMT cladding over conventional thermal spray is the lower processing temperature of the former, which has a correspondingly smaller thermal impact on the processed materials (Ref 2). Therefore, CMT cladding is especially useful for coatings that are susceptible to oxidation at high temperature. CMT cladding has been employed for cladding cobalt (Ref 3-5), nickel (Ref 6-11), aluminum (Ref 12, 13) and ferrous alloys (Ref 11, 14). Dense claddings with reduced oxidation provide superior mechanical, thermal and electrical properties (Ref 15, 16). On the negative side, it also results in residual tensile stresses as a result of differential thermal expansion (Ref 16), although some kinetic processes may tend to produce residual compressive stresses on the surface (Ref 17, 18). A reduction in ductility after cladding is also not uncommon. To mitigate the negative effect of the CMT cladding, heat treatment may be employed. Heat treatment is in vogue for CMT welding (Ref 19-21). The improved strength and hardness of the aged AA 2024 joint could be obtained thanks to refined grain structure (Ref 19). The heat treatment resulted in enhanced tensile strength and hardness of AA6061 welded joint because of fine and homogenous distribution of precipitates (Ref 20). The heat treatment could restore the weld strength of aluminum to zinc-coated low carbon steel, which

had reduced due to heat-affected zone softening (Ref 21). The microstructure and the mechanical properties of cold-sprayed copper (Ref 15, 16, 22), aluminum (Ref 23), stainless steel (Ref 24, 25), titanium (Ref 26) and Inconel 718 (Ref 27) coatings could be altered by heat treatment. The thermal and electrical properties of the cold-sprayed coatings enhanced as a result of improved particle-to-particle contact, but the hardness reduced owing to the absence of work hardening from annealing heat treatment (Ref 15, 22). Additionally, heat treatment could reduce the porosity of cold-sprayed coatings (Ref 25) and even in bulk materials (Ref 16).

In a recent work (Ref 28), Fe-based ER70S-6 electrode was cladded on aluminum (Al) substrate using CMT technique. The review of the literature reveals that while there have been some studies on heat treatment after cold spraying, there is no article on heat treatment for cladding of Fe-based electrode on aluminum using CMT. This work fills up that gap to find out the effect of heat treatment on the porosity, microstructure, surface roughness and mechanical properties of cladded layer. In the present work, the effect of heat treatment on the cladded layer is studied. Following four types of heat treatment were used: (1) sample heating up to 600 °C followed by a 1-h holding and furnace cooling for 24 h, (2) sample heating up to 600 °C followed by a 1-h holding and water quenching, (3) artificial age hardening by heating the sample up to 175 °C, holding it for 24 h and then furnace cooling for 6 h and (4) deep cryo-treatment by dipping the sample in liquid nitrogen (−196 °C) for 1 h and then bringing to ambient temperature. A detailed comparative study of these types is presented, and the best type is identified.

2. Materials and Methods

In this study, the substrate material was taken in the form of 180 × 100 × 6 mm size plates of AA 6061-T6 alloy. This aluminum alloy is frequently employed in structural applications due to its high specific strength and good corrosion resistance. ER70S-6 filler rod of 1.2 mm diameter was used for cladding, which was purchased from ESAB, India. The typical weld metal analysis as supplied by ESAB was of 1.5% Mn, 0.9% Si, 0.01% S, 0.07% C, 0.30% Cu, 0.013% P, traces of Cr, Mo, Ni, Al and V and the rest Fe by weight. The microstructure and in-house EDS elemental composition of filler rod are shown in Fig. 1(a) and (b), respectively. The substrate composition was of 0.1% Ti, 0.3% Fe, 0.3% Zn, 0.7% Si, 0.7% Cu, 0.7% Cr, 1% Mg by weight and the rest Al, as reported in (Ref 28). A Fronius make TPS400i CMT machine was used for the cladding. The speed and route of the cladding layer were changed using a 6-axis FANUC make Arc Mate 100iD robot.

2.1 Cladding Process

The electrode wire was kept perpendicular to the top surface of the aluminum plate for deposition by melting. The electrode traversed along length direction; direction of traverse was kept same in all the passes. Overlapping percentage between two tracks was 20%. The cladding was carried out in the room temperature. Prior to the cladding procedure, the substrate plate was thoroughly cleaned with acetone. The heat input Q during cladding was 142.5 J/mm, as calculated by

$$Q = \eta \left(\frac{VI}{S} \right), \quad (\text{Eq 1})$$

where η is the efficiency, which is about 0.95 (Ref [29]), V the voltage at 10 V, I the current at 100 A and S is the welding speed at 400 mm/min. Cladded thickness was about 3 mm.

2.2 Sample Preparation

Cladded portion was milled about 1 mm to remove the uneven surface. The final thickness of the cladding was 2 mm. Its top surface is the focus of the study. Different samples were cut into sections using a wire-cut electrical discharge machine (WEDM) for microstructure and mechanical characterization purpose. Figure 1(c, d) shows the experimental setup and a sectioned sample for the characterization. Cladding direction (direction of electrode traverse) is along the length of the sample.

2.3 Heat Treatment Process

The samples were properly cleaned with acetone before the heat treatment process to remove the undesired oils and dirt during the cutting process using WEDM as well as milling. The heat treatment was carried out using an electric muffle furnace. The heat treatment used on the extracted samples was of four types—(1) sample heated up to 600 °C followed by a 1-h holding and furnace cooling in 24 h, (2) sample heated up to 600 °C followed by a 1-h holding and water quenching, (3) artificial age hardening by heating the sample up to 175 °C, holding it for 24 h and then furnace cooling in 6 h and (4) deep cryo-treatment (DCT) by dipping the sample in liquid nitrogen (−196 °C) for 1 h and then bringing to ambient temperature.

Ming et al. (Ref 24) reported the enhancement of mechanical properties of 304 stainless steel coating with heat treatment at 600 °C for 1 h. A temperature more than 600 °C is likely to start melting in base metal at certain location. Thus, the temperature in Type 1 and Type 2 heat treatment is limited to 600 °C. In Type-3 heat treatment, viz. artificial age hardening, temperature was kept at 175 °C, considering that aging temperature for aluminum alloy is generally kept in the range 100–200 °C. Type-4 heat treatment was used to transform retained austenite into hard martensite.

2.4 Porosity Analysis

The porosity of the different samples was calculated according to Archimedes' principle. Sectioned sample of 10 × 10 × 8 mm size was properly cleaned and weighted for the dry weight. The same sample was dipped in the distilled water for 24 h, which was dried with tissue paper to remove the water before weighing for the saturated weight. It was then dipped in water and weighted for the suspended weight. The accuracy of the weight measurement was 0.01 mg on a digital weight machine. According to Archimedes' principle, the porosity is given by

$$\varepsilon = \frac{W_{\text{sat}} - W_{\text{dry}}}{W_{\text{sat}} - W_{\text{susp}}} , \quad (\text{Eq 2})$$

where W_{dry} is the dry weight, W_{sat} is the weight of the saturated sample, i.e., weight after soaking in distilled water for 24 h, and W_{susp} is the weight of the suspended sample in water.

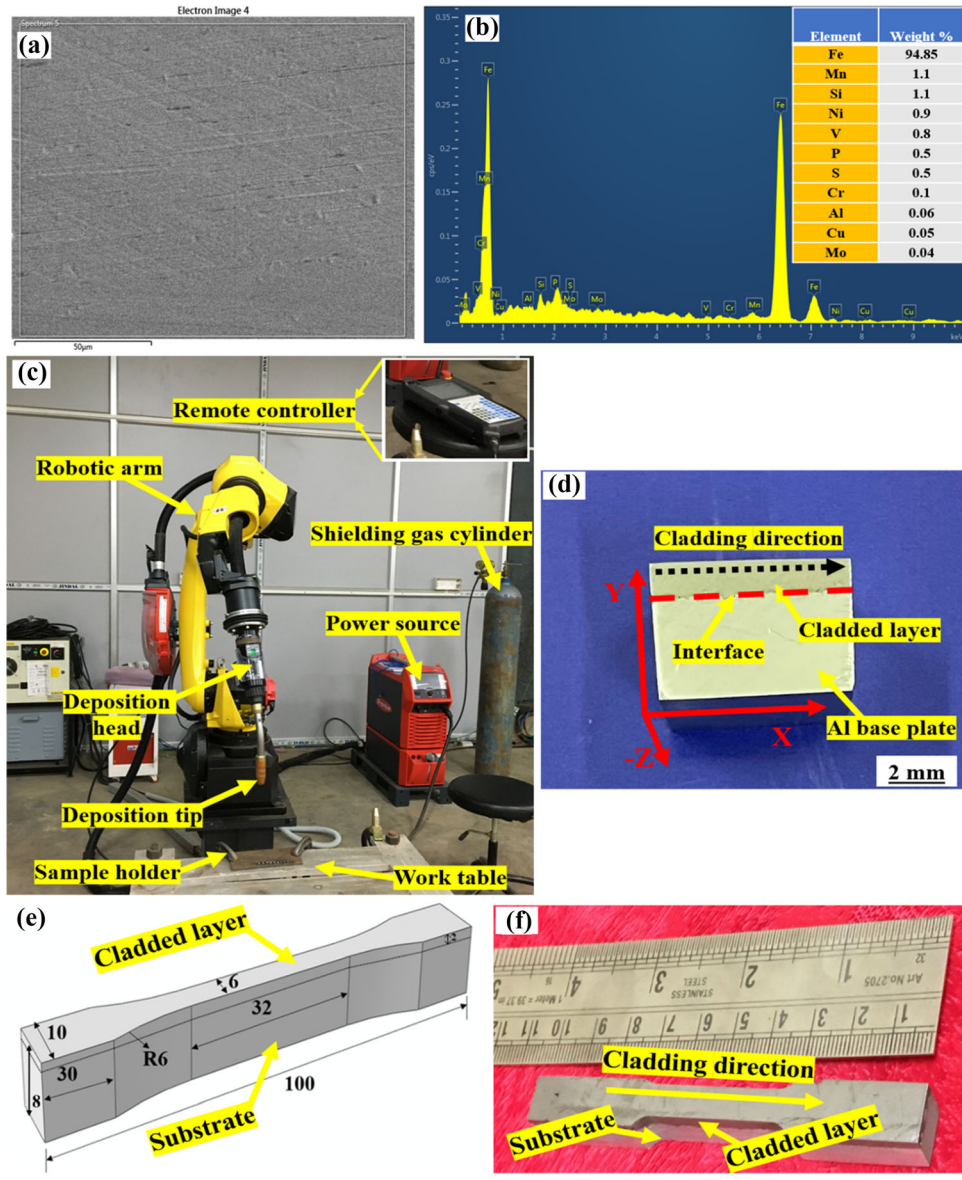


Fig. 1 EDS analysis of electrode (acting as filler rod): (a) microstructure of filler rod (X250) and (b) elemental distribution; experimental setup for deposition of cladding layer using CMT technology: (c) experimental setup and (d) sectioned wire cut and milled sample for different characterization prior to heat treatment; tensile specimens: (e) schematic diagrams and (f) sectioned wire cut sample for tensile characterization

2.5 Microstructural Analysis

Using silicon carbide sheets with grit sizes ranging from 80 to 2000 to polish the sectioned samples, cloth and diamond polish were applied. The polished samples were etched into Nital reagent for 15 s in order to observe the microstructure. The Nital reagent contains 5 ml of nitric acid (HNO_3) and 95 ml of alcohol (CH_3OH). The upright optical microscope was used to produce the optical micrographs. Field emission scanning electron microscopy (FESEM) was used to examine the surface, worn-out debris and fracture morphology at operating voltage of 20 kV. A gold-sputtered coating was applied to the samples before FESEM. Using ImageJ software and the random line intercept approach, the samples grain size was calculated. Intercept lines were positioned such that at least 10 grains are intercepted by the lines. The grain size analysis was conducted at the top surface of the cladded layer.

2.6 Surface Roughness Analysis

The sample size of $10 \times 10 \times 2 \text{ mm}^3$ was scanned through a non-contact atomic force microscopy (AFM) to examine the surface roughness of the cladded layer (Model: Cypher S; Make: Oxford Instruments) in tapping mode along the cladding direction of rod path. The test was conducted on the surface of the cladded layer before surface milling, i.e., as-cladded condition. The average scan data of three different scanning test of $10 \times 10 \mu\text{m}^2$ are reported.

2.7 XRD Analysis

The x-ray diffraction (XRD) study of the different samples was carried out using Rigaku x-ray diffractometer with $\text{Cu}-\text{K}\alpha_1$ radiation ($\lambda = 1.54056 \text{ \AA}$). To identify the phases contained in the samples, x-ray diffraction investigations were conducted. The solid sample was placed on a sample holder with

dimensions of $20 \times 25 \times 2$ mm³. The measurements were taken at an applied voltage of 45 kV, grazing incidence angle of 1° and a current of 200 mA, while the samples were scanned at a rate of 20°/min with steps of 0.05° in the diffraction angle (2θ) range of 30°-90°. Estimated penetration depth calculated from *X'Pert HighScore Plus* software (Ref 30) for 0.4 packing is about 0.4 μm, which is sufficient to study the surface properties. This value is sensitive to packing, which was not measured precisely. Hence, penetration depth of 0.4 μm should be treated as a rough approximation only. The x-ray diffractogram produced by the experiment demonstrates the connection between relative intensity and diffraction angle. The interplanar spacing d corresponding to each peak is utilized for identifying the various phases of the material. By comparing experimental d -values with standard reference cards from the Joint Committee of Powder Diffraction Standard (JCPDS) file, the phases contained in the samples were determined. Crystallite size and lattice strain are estimated from the peak position and peak broadening from the XRD pattern. By adopting a precise lattice parameter computation method, the lattice parameter is computed from the x-ray diffraction pattern.

2.8 Hardness Analysis

Vickers microhardness of samples was conducted using MVH-II (Make: Omni Tech) microhardness tester. The hardness analysis has been conducted at the top surface of the cladded layer. Using a 136° square-based Vickers diamond pyramid, an indentation was created with a 200-g load and 20-s dwell period. The samples were polished such that their opposing surfaces were parallel to each other. Ten indentations were carried out on each sample, and the average microhardness hardness value and standard deviations are reported. It was ensured that the indentations were at a distance that was at least twice the preceding indentation's diagonal length. The microhardness value was calculated as

$$HV = 1.8544 \frac{P}{d^2}, \quad (\text{Eq } 3)$$

where P is the applied load and d is the diagonal length of indentation.

2.9 Wear Analysis

Pin-on-disc dry sliding wear tests were performed on steel discs with a hardness of 64 HRC in pin-on-disc with applied normal load of 20 N and a fixed sliding speed of 350 rpm. In the wear test, the relative sliding was along the cladding direction of electrode. The hardened steel was 100 mm in diameter and 10 mm thick. The steel disc surface was properly cleaned with acetone to remove any foreign particles which may act as a hard impurity against pin surface. Cladded material in the shape of 10 mm diameter pin traversed on 70 mm track diameter on disc, in accordance with ASTM standard: G99. The weight loss, wear volume and coefficient of friction (CoF) were calculated as follows:

$$W_{\text{loss}} = W_1 - W_2, \quad (\text{Eq } 4)$$

where W_1 and W_2 are the weight of the sample before and after wear, respectively,

$$\text{Wear volume loss} = \frac{W_{\text{loss}}}{\text{density of cladded layer}}, \quad (\text{Eq } 5)$$

$$\text{CoF} = \frac{\text{frictional resistance}}{\text{normal load}}. \quad (\text{Eq } 6)$$

The sliding speed is given by

$$\text{sliding speed} = \frac{\pi DN}{60}, \quad (\text{Eq } 7)$$

where $D = 70$ mm is the track diameter and $N = 350$ rpm is the number of revolution/min by the pin on hardened steel surface. Product of sliding speed and time provides sliding distance. For a 30 min of wear test, the sliding distance was 2309 m.

The load was imparted to the sample during sliding via a cantilever mechanism, and the specimens were brought into close proximity to the rotating disc at a track diameter of 70 mm. Prior to and following each test, the samples were weighted using a digital microbalance to an accuracy of 0.01 mg. The wear rate was calculated from the weight loss information in terms of volume loss per unit sliding distance. Based on the applied load and the observed frictional force, the coefficient of friction was calculated. The worn surface 3D morphology and roughness was analyzed by AFM at 3 different areas of squares 30 μm side, and the average value is reported. On the steel disc, sticking of the dislodged material from the specimen surface was also observed. The worn debris from the steel surface was also collected for the characterization purpose.

2.10 Tensile Property Analysis

The tensile specimen was sectioned according to the ASTM E8M-11 standard. However, 2 mm thickness got increased due to cladding layer. The test was conducted using Autograph AGX-V universal testing machine with 0.1×10^{-3} s⁻¹ strain rate. The test was conducted at room temperature. For the fracture morphology, height of ~2 mm just below the fracture spot was sectioned. Figure 1(e, f) shows the schematic and wire cut sample for the tensile characterization.

3. Results and Discussion

In this section, effects of heat treatment are reported. The term as-cladded means samples obtained after milling the cladded samples for about 1 mm depth, unless mentioned otherwise. Heat treatment was also carried out on cladded and milled samples. However, while studying the effect of heat treatment on surface roughness, milling was not carried out.

3.1 Porosity Study

Figure 2 shows the porosity percentage of the as-cladded and heat-treated samples. The as-cladded sample had the maximum porosity of 2.56%. The porosity in the cladded samples reduced to 0.48-1.21% after heat treatment. Type 1 heat treatment provided 1.35% porosity, the least among all samples due to sintering effect. Bin-you et al. (Ref 31) also reported 19% reduction in porosity during annealing at 600 °C of Fe-based 1-mm cladding layer through spray technique. In the present study the porosity has reduced by 47% at similar annealing temperature and the cladding layer thickness of 2 mm.

Figure 3 shows typical cross-sectional optical micrographs of the cladding layer for various samples. The micrographs were obtained from the plane containing thickness and cladding directions, i.e., from the front view of the sample. The

micrographs depict the high dense nature of the claddings with uneven infiltration of cladding materials into base metal due to differences in density. The as-cladded layer depicts presence of small oxide strings and microcracks. However, in case of heat-treated samples pores and micro-cracks reduced.

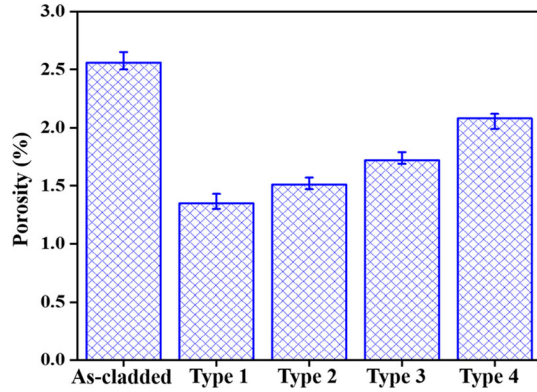


Fig. 2 Porosity of the sample before and after heat treatment process

3.2 Microstructural Study

The FESEM morphology of the cladded layer after cladding depicts development of different phases such as ferrite, martensite and distribution of carbides discussed in (Ref 28). The different phases occurred due to the fast heating and cooling involved in CMT cladding process. The cladding layer cools in a manner analogous to quenching, where martensite transformation takes place at various places in the structure. However, due to application of different types of heat treatment to the cladded layer the proportion of the developed phase in the heat-treated layer has been changed to some extent as compared to as-cladded layer. The proportion of martensite transformation during the heat treatment process was calculated by image area method. The martensitic phase at the as-cladded layer was $\sim 32\%$, which reduced to $\sim 20\%$ in Type 1 heat treatment and $\sim 26\%$ in Type 3 heat treatment. However, in

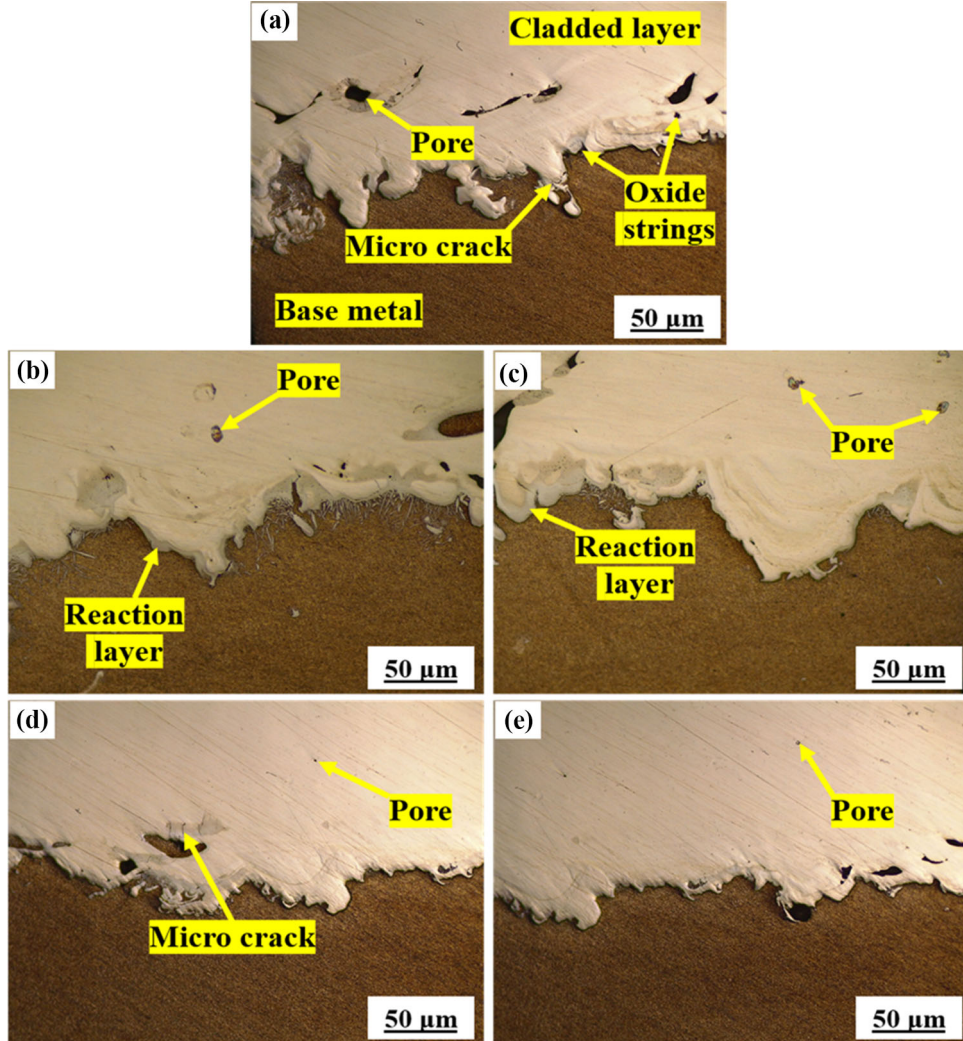


Fig. 3 Cross-sectional morphology (front view) of cladded (and milled) layer and substrate: (a) as-cladded, (b) Type 1, (C) Type 2, (d) Type 3 and (e) Type 4

Type 2 and Type 4 heat treatment, the martensitic phase transformation increased to $\sim 43\%$ and $\sim 56\%$, respectively. The results are also relatable in the visible observation of the surface morphology in the X-Y plane (Fig. 4b, d, f, h). The martensite phase is densely distributed in the Type 4 heat-treated sample compared to all other types of heat-treated sample.

Distinct grain boundary is visible in the X-Z plane morphology (Fig. 4c, e, g, i). The ferritic phase and distribution of coarse carbide is dominant in Type 1 and Type 3 heat-treated sample. During Type 1 heat treatment, the high temperature causes the primary alloy carbides to dissolve more thoroughly, adding additional carbon and alloying components. This led to the formation of a network of tiny coarse carbide precipitate at the grains during cooling. However, the proportion is low in Type 3 owing to heat treatment at lower temperature. At a few region pearlite and cementite phases were also developed in Type 1 and Type 3 heat-treated sample due to slow cooling. The proportion of ductile ferritic phase is dominated by brittle acicular martensite phase in Type 2 and Type 4 heat-treated sample. Some retained austenite structure was observed in Type 2 heat-treated sample. However, in Type 4 heat treatment no such phase was observed. Type 4 heat treatment also reduced the proportion and distribution of carbide precipitates. Harish et al. (Ref 32) also observed the same in cryogenic treating of EN 31 bearing steel.

Figure 5 shows the EDS analysis of Type 1 heat-treated sample. The cross-sectional micrograph (Fig. 5a) depicts good bonding between cladded layer and substrate without any visible porosity. The area EDS elemental distribution (Fig. 5b) shows the presence of elements throughout the sample. The line EDS analysis (Fig. 5c) in the interface region shows only slight hike in the oxygen present, which is indicative of less oxidation during cladding using CMT process. The elemental maps depict uneven distribution of elements in the cross section (Fig. 5d).

3.3 Grain Size Analysis

Figure 6 shows the microstructure of the as-cladded and heat-treated samples. Grains contain mostly martensite along with other phases. Some grains contain traces of the retained austenite. The heat treatment type had a significant impact on the grain size. With the increasing temperature the grains size also increased. The average grain size increased during Type 1 and Type 3 heat treatment, which was 30 and 29 μm , respectively, against 27 μm in the as-cladded sample. Low temperatures result in irregular grain shapes and curved grain boundaries, whereas high temperatures result in roughly hexagonal grain shapes and flat grain boundaries (Ref 33). The similar observation is also observed in Fig. 6. The maximum reduction in the average grain size was observed in case of Type 4 heat treatment; the average grain size was 20 μm . It is because carbon content has a significant impact on the movement and dissolution of components during the modification of microstructure. Due to the migration and dissolution of the carbon during Type 4 heat treatment, the phase modification (martensite) in the steel cladding occurred. The stress developed by the lattice shrinkage of martensite during cryogenic treatment encourages the migration of moveable dislocations, which results in grain refinement (Ref 34). Li et al. (Ref 35) also reported that cryo-treatment effects significantly the low-angle and high-angle grains boundary and their average influences result in grain refinement. Figure 7

shows the distribution of the grain size of the as-cladded and heat-treated samples. Significant amount of small size grains ($< 20 \mu\text{m}$) are observed in Type 4 heat treatment unlike all other types of heat treatment.

3.4 Surface Roughness Study

Figure 8 shows 3D surface profile of as-cladded (without milling) and heat-treated (without milling) samples. The surface roughness value increased to 75 nm in Type 1 heat-treated sample, compared to 46 nm in the as-cladded sample. The increase in surface roughness value for Type 1 heat-treated sample is mainly due to the increased grain size. At high temperature, the formation of coarse carbide and the oxide layer has major role in enhancing roughness value. However, during Type 4 heat treatment, the formation of fine carbide, absence of oxidation and grain refinement led to minimum surface roughness, which was 25 nm. However, the surface roughness value is dependent on surface area and cutoff length (Ref 36). The present scan surface area was 100 $(\mu\text{m})^2$.

3.5 XRD Study

The phases developed in the cladded layer under various heat treatment conditions have been investigated using XRD analysis, and the results are shown in Fig. 9. The plots depict the development of crystalline and amorphous phases in the cladded layers. The pattern shows the presence of α -Fe (ferrite, BCC) phase as dominant phase and a few traces of γ -Fe (retained austenite, FCC) phase, which is consistent with the FESEM micrograph observed in Fig. 7. The intensity of the γ -Fe reduced in Type 4 heat-treated sample, confirming the transformation of retained austenite to martensite. Additionally, as evident from Fig. 9, the heat treatment changes the intensity of the peaks across all crystallographic planes and angles. After heat treatment, the big hump pattern diminished and the peaks moved in the direction of an increasing angle. This confirms the change in the matrix structure and strain state as a result of heat treatment (Ref 31).

Figure 10(a, b) shows the crystallite size and lattice strain of the as-cladded and different heat-treated samples. The crystallite size and the lattice strain are calculated using Williamson-Hall equation (Ref 37):

$$\beta = \beta_G + \beta_S \quad (\text{Eq } 8)$$

$$\beta_G = \frac{K\lambda}{D \cos \theta} \quad (\text{Eq } 9)$$

$$\beta_S = 4\varepsilon \sin \theta \quad (\text{Eq } 10)$$

where β is the full width half maxima (FWHM), β_G is the contribution due to crystallite size, β_S is the contribution due to lattice strain, $K = 0.9$ is the constant, λ is the wavelength, D is the crystallite size, and ε is the lattice strain. The lattice strain ε was calculated by rearranging the Williamson-Hall equation as

$$\beta \cos \theta = \frac{K\lambda}{D} + 4\varepsilon \sin \theta. \quad (\text{Eq } 11)$$

Crystallite size and lattice strain are determined from intercept and slope of the linear plot of $4\sin\theta$ and $\beta\cos\theta$. Figure 11(a) shows a linear plot of Type 4 heat-treated sample. The maximum crystallite size of 47.16 nm was observed in case of Type 1 heat-treated sample, while the minimum was 30.53 nm in Type 4 treated sample against 38.94 nm in the as-

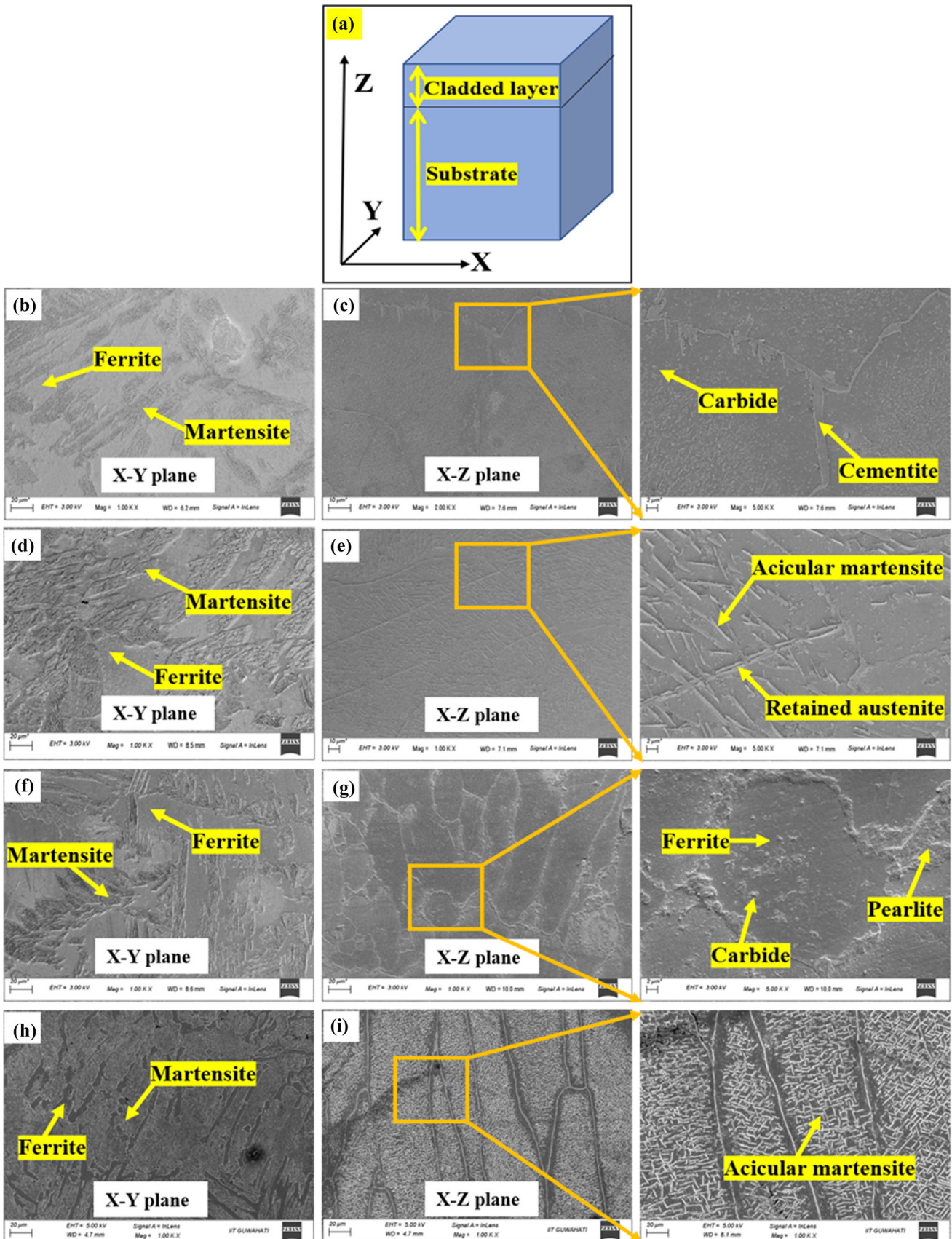


Fig. 4 Morphology at the top surface (X – Y plane) and at the cross section (X – Z plane) of cladded (and milled) layer: (a) schematic showing X-Y-Z-axes, (b, c) Type 1, (d, e) Type 2, (f, g) Type 3 and (h, i) Type 4. X- and Z-axes are along cladding and thickness directions, respectively

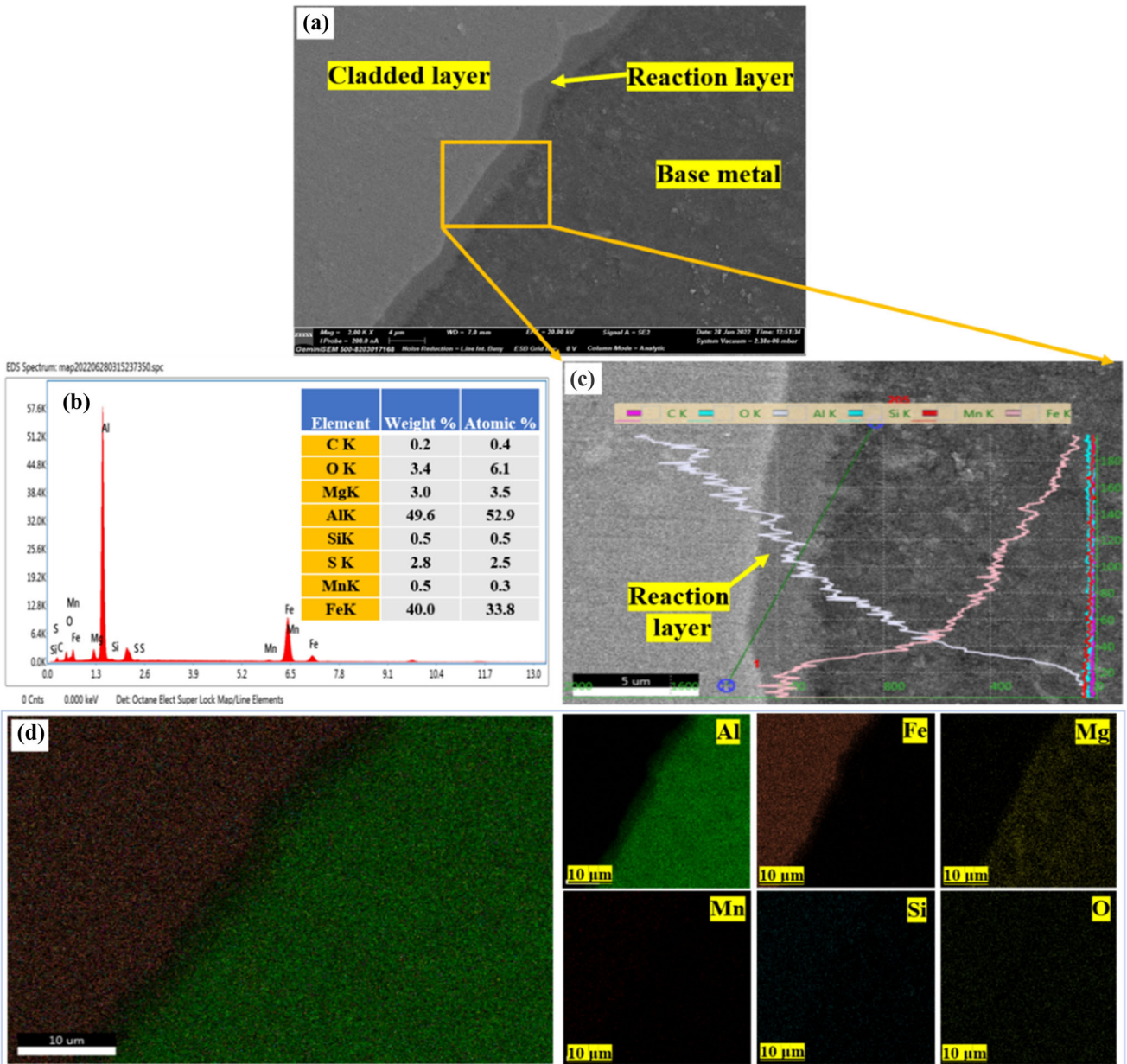


Fig. 5 EDS analysis of Type 1 heat-treated cladded (and milled) layer: (a) cross-sectional morphology, (b) elemental distribution, (c) cross-sectional interface elemental graphs and (d) maps of present elements

cladded layer. In Type 1 samples, heat treatment was carried out at higher temperature. Higher temperatures facilitate atomic vibration and diffusion, forming grains with lower surface energy (Ref 38); critical sizes of the nuclei rises (Ref 39).

Figure 10(c) shows the dislocation density of the a as-cladded and different heat-treated samples. The dislocation density (ρ) is calculated as (Ref 40):

$$\rho = \frac{2\sqrt{3}\epsilon}{Db} \quad (\text{Eq 12})$$

where b is burger vector, for BCC structure $b = (a\sqrt{3})/2$, where a is the lattice parameter. It was computed from three highest XRD peaks of different samples using the Nelson–Riley extrapolation method. For each peak, the fraction error is given by the product of a constant K and a trigonometric function called Nelson–Riley function (Ref 37). Thus,

$$\frac{\Delta a}{a} = K \left(\frac{\cos^2 \theta}{\sin \theta} + \frac{\cos^2 \theta}{\theta} \right). \quad (\text{Eq 13})$$

The error will be zero when the value of Nelson–Riley function is zero. In that case, the value of lattice parameter calculated on the basis of Bragg's law will be the exact value. However, there are no data for zero value of Nelson–Riley function. It is customary to extrapolate the value of a for zero value of Nelson–Riley function. For this purpose, a is plotted against the value of Nelson–Riley function with a linear fit. The point of intersection of the fitted line with the axis corresponding to a provides the actual lattice parameter value, which is shown Fig. 11(b) for Type 4 treated sample; it is 2.865 Å.

Following the aforesaid procedure, the maximum dislocation density of $10.78 \times 10^{16}/\text{m}^2$ was observed in case of Type

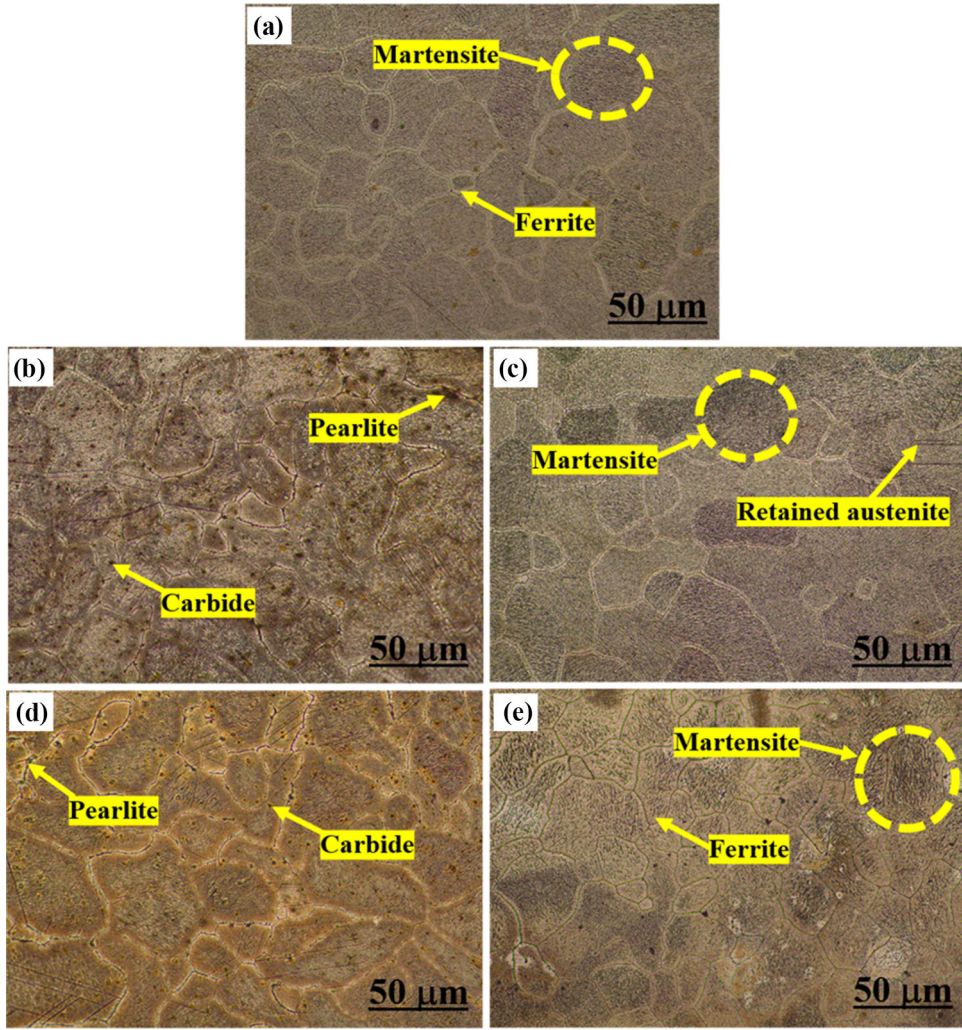


Fig. 6 Optical micrograph at the top surface of cladded (and milled) layer (X20): (a) as-cladded, (b) Type 1, (C) Type 2, (d) Type 3 and (e) Type 4

4 heat-treated sample, while the minimum was $4.15 \times 10^{16}/\text{m}^2$ in Type 1 treated sample. For as-cladded samples, dislocation density was $6.08 \times 10^{16}/\text{m}^2$. The dislocation density is related to crystallite size. The dislocation density increases with decrease in crystallite size. However, thermal expansion also plays a major role in dislocation density of Fe-C alloys by changing the concentration of carbon content (Ref 41). With the decrease in the temperature, differential local thermal expansion causes localized stress to rise, which multiplies dislocations (Ref 42). Since the distribution of carbon inside the microstructure is heterogeneous, it is proposed that this will cause local lattice strain and dislocation multiplication during Type 4 heat treatment. The crystallite size, lattice strain and dislocation density of the electrode (acting as filler rod) were 56.82 nm, 0.13 and $3.41 \times 10^{16}/\text{m}^2$, respectively. The maximum crystallite size and minimum dislocation density observed in the filler rod owe to non-occurrence of any mechanical alteration to the property.

3.6 Hardness Study

The Vickers microhardness value of the as-cladded sample and heat-treated sample is presented in Fig. 12. The variation of hardness in the Fe-based coating is due to the effects of

strengthening mechanisms such as grain boundary strengthening, solid solution strengthening, precipitation strengthening, transformation strengthening and dislocation strengthening. Optical micrographs in Fig. 6 reveal that type of heat treatment affects grain size. In general, the heat treatment involving high temperature results in grain coarsening. Type 4 heat treatment dealing with cryogenic temperatures results in refined grains. Grain size appears to be the most influencing factor on hardness. The highest value of hardness is 407 HV for Type 4 heat-treated cladding layer with 20 μm grain size, while the lowest value of hardness is 181 HV for Type 1 heat-treated cladding layer with 30 μm grain size. The high density of grain boundaries in the fine-grained structure acts as a barrier to the motion of dislocations causing the rise in microhardness (Ref 43). The grain-boundary strengthening mechanism is captured by the Hall-Petch relation (Ref 44, 45):

$$H = H_0 + \frac{k_H}{\sqrt{d}}, \quad (\text{Eq } 14)$$

where H_0 and k_H are material constants, H is the hardness, d is the average grain diameter. In order to assess the effectiveness of this relation, constants H_0 and k_H are obtained from the average grain size and hardness data of Type 1 and Type 4 heat

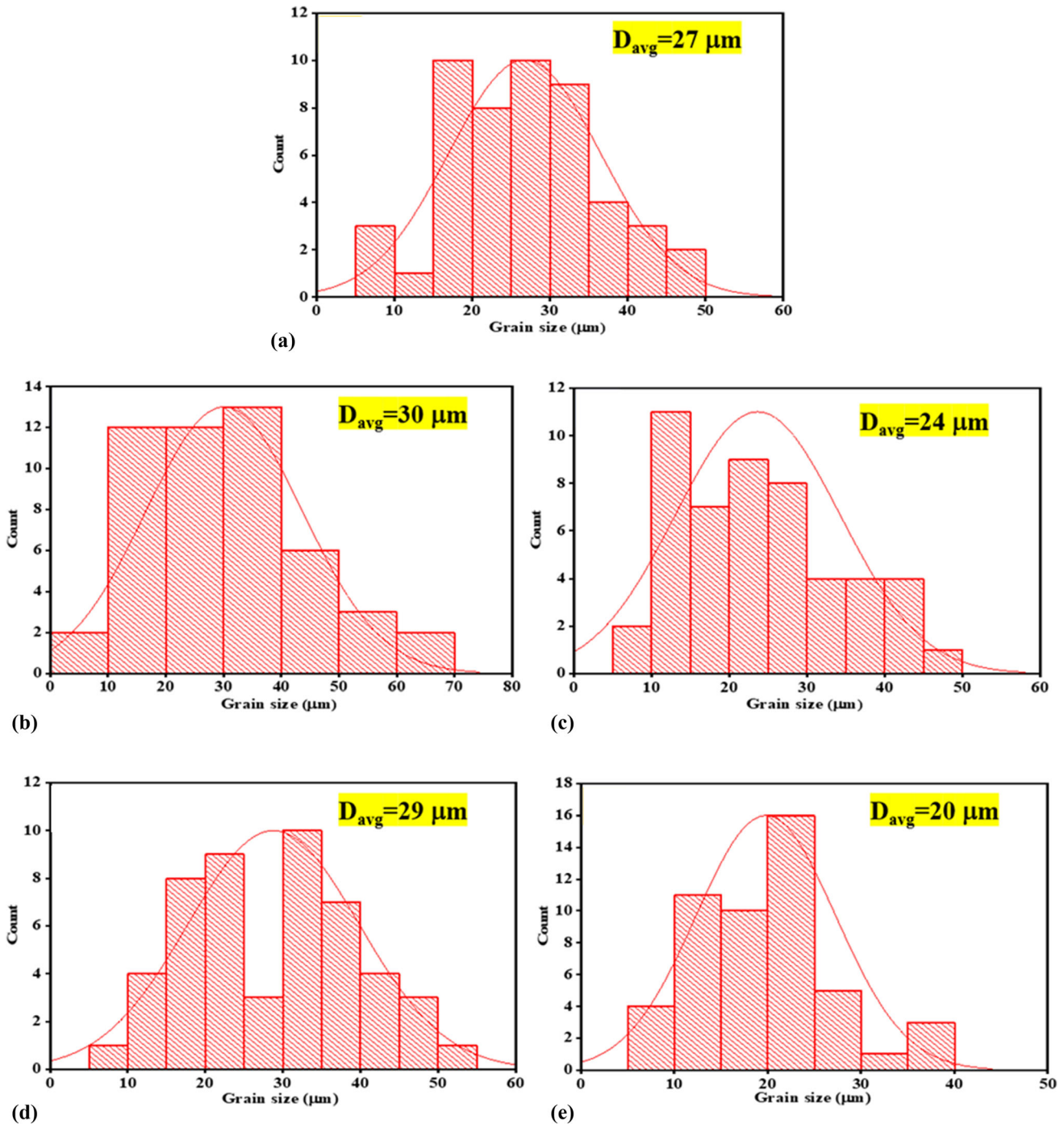


Fig. 7 Grain size plot of cladded (and milled) layer (based on top surface): (a) as-cladded, (b) Type 1, (C) Type 2, (d) Type 3 and (e) Type 4

treatment. These two types of heat treatment represent two extremes in terms of hardness. Hardness values in Type 2 and Type 3 heat treatment as well as in as-cladded case lie between the values obtained from Type 1 and Type 4. Any data-fitting technique predicts well in interpolation, but produces large error in extrapolation. Hence, the values of d and H were substituted in Eq. (14) to get two simultaneous linear equations based on the average values from Type 1 and Type 4 heat treatment. Accordingly, $H_0 = -783$ MPa and $k_H = 5290$. With these values, the calculated (interpolated) hardness values are 240 HV, 304 HV and 203 HV for as-cladded, Type 2 and Type 3 specimens, respectively. Corresponding measured

hardness values are 237 HV, 331 HV and 204 HV, which show very good agreement with the calculated values. However, negative value of H_0 is untenable from the physics point of view because it represents the hardness of a highly coarse-grained material and should be a non-negative value. Despite this logical inconvenience, Hall-Petch relation is providing good estimate of hardness.

According to FESEM morphology (Fig. 4), the difference in microhardness value due to heat treatment is also caused by transformation strengthening. The maximum hardness value for Type 4 and Type 2-treated cladding layer owes to the strong and hard martensite structure compared to other types of

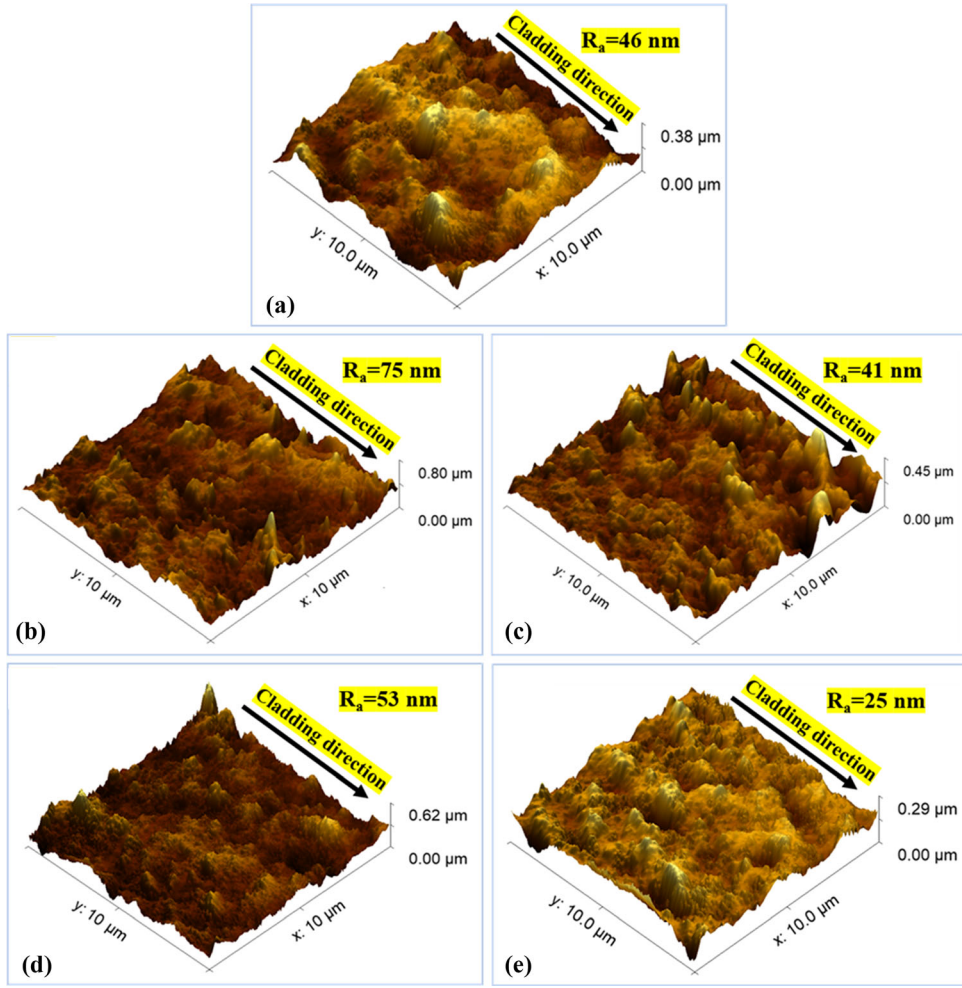


Fig. 8 AFM 3D surface micrograph of cladded (without any post-processing) layer prior to milling: (a) as-cladded, (b) Type 1, (C) Type 2, (d) Type 3 and (e) Type 4

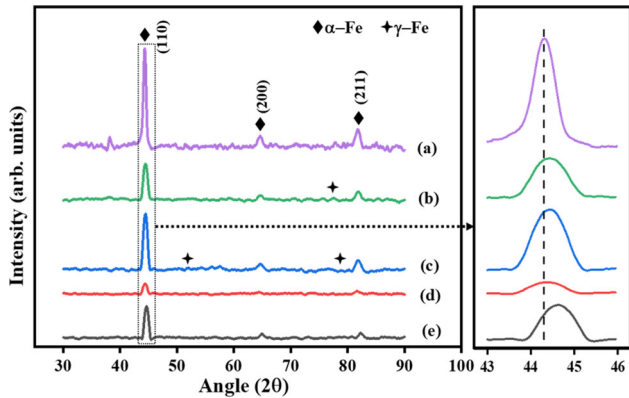


Fig. 9 XRD plot at the top surface of cladded (and milled) layer: (a) as-cladded (Ref 28), (b) Type 1, (C) Type 2, (d) Type 3 and (e) Type 4

specimens. Das et al. (Ref 46) stated that cryogenic heat treatment increases the dislocation and twin boundary in the specimen and C atoms precipitates from the martensite matrix to produce fine carbides with other alloying elements. However, due to presence of soft retained austenite and carbide at a few places and lower proportion of martensite transformation in the

Type 2-treated cladding layer, the hardness value is low as compared to Type 4 treated cladding layer. The hardness value of Type 1 and Type 3 heat-treated cladding layer is lower than that of the as-cladded layer due to ferritic transformation. The quantitative effect of transformation strengthening is not studied in this work. Its incorporation in Hall–Petch relation may resolve the problem of negative H_0 , which aspect will be investigated in a future work.

3.7 Effect on Friction

The dry-sliding test was carried out against hardened steel at room temperature. The variation of coefficient of friction (CoF) of the heat-treated samples is shown in Fig. 13. The average CoF in the as-cladded layer was 0.23 under similar test condition (Ref 28). The average CoF value increased to 0.26 in the Type 1 heat-treated sample and reduced to 0.20 in the Type 4 heat-treated sample. The high CoF in Type 1 heat-treated samples is due to its low hardness. Furthermore, the contact surface becomes softer as a result of frictional heat developed between the Type 1 heat-treated sample and hardened steel during the dry sliding wear. As a result, at the contact surface the debris forms, which increases the CoF value due to plowing and abrasion (Ref 47). The development of coarse carbide also aids in increasing CoF for Type 1 and Type 3 heat-treated

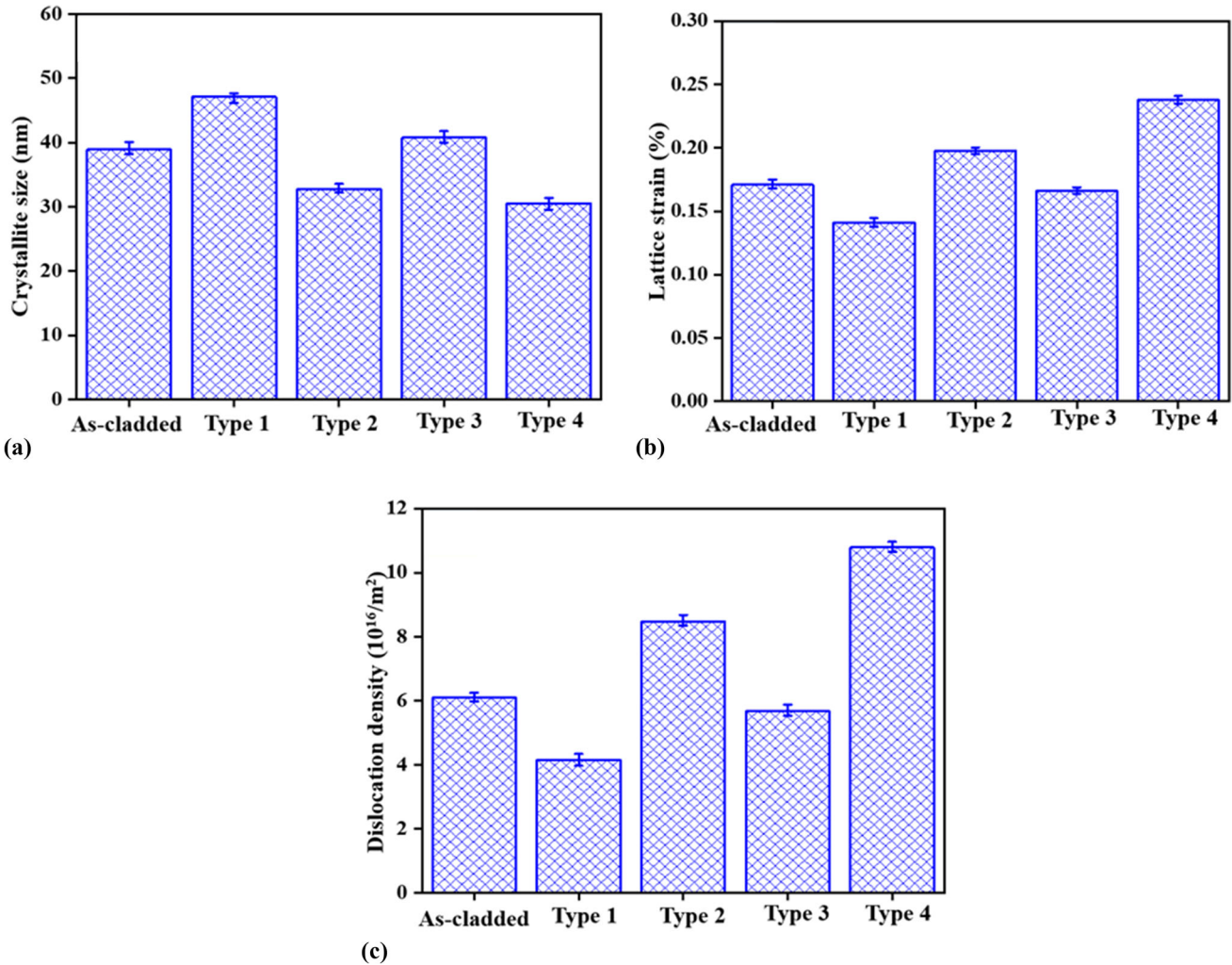


Fig. 10 XRD analysis of cladded (and milled) layer: (a) crystallite size, (b) lattice strain and (c) dislocation density

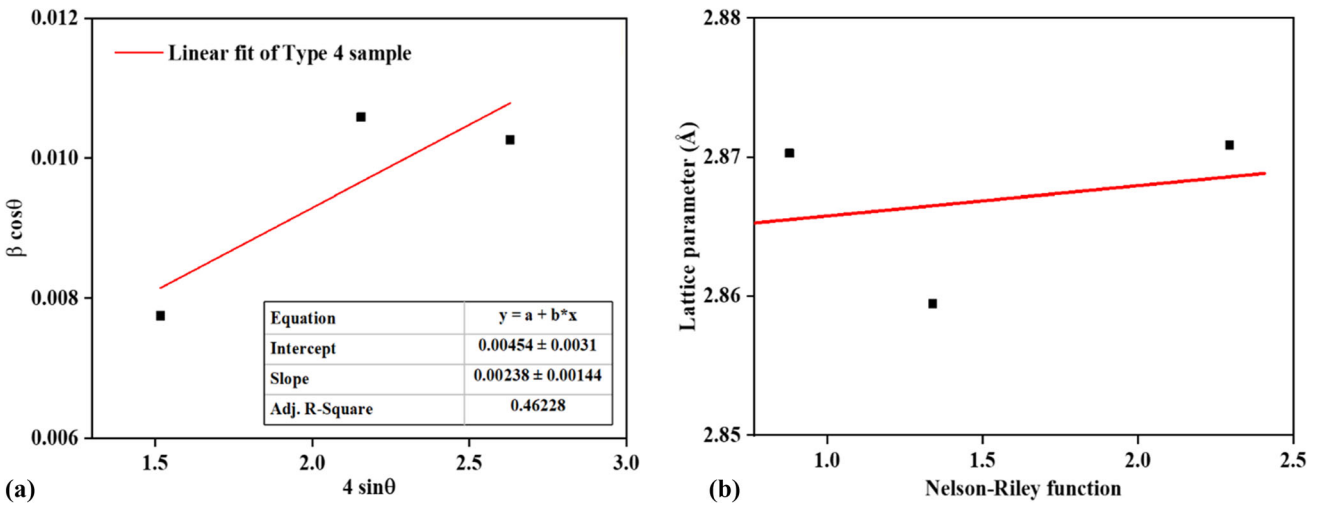


Fig. 11 XRD analysis of Type 4 heat-treated sample: (a) linear plot and (b) lattice constant from Nelson–Riley function

sample. During Type 4 heat treatment the development of carbide is slow and uniformly distributed hard martensitic structure is formed (Fig. 4), leading to reduction in debris and consequently friction. Moreover, a harder surface encounters

less frictional resistance as it provides less adhesive contact area for a given load (Ref 48).

The 3D AFM morphology of the worn surface is shown in Fig. 14. The wear tracks, debris, grooves and the pits are visible

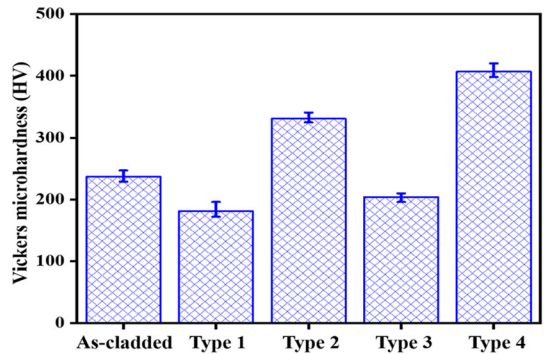


Fig. 12 Variation of microhardness at the top surface of cladded (and milled) layer due to heat treatment

in the morphology. The sudden hike in the peak is due to wear debris and valleys are due to groove, pits and tracks. The morphology suggests that significant plastic deformation had

occurred during wear. The Type 4 heat-treated sample surface had smallest hike in peak-to-valley distance compared to all samples. The minimum average surface roughness (R_a) value of 76 nm was observed in Type 4 heat-treated sample surface, and the average maximum R_a was 126 nm in Type 1 heat-treated sample surface compared to as-cladded sample surface, which was 94 nm. The greater increase in R_a value is related to the CoF. The smooth surface due to enhanced hardness and low plastic deformation in the Type 2 and Type 4 heat-treated sample results in low R_a value. The surface roughness was measured in the scan surface area of 900 (μm)².

3.8 Wear Study

The wear mass loss of the as-cladded sample and heat-treated sample is depicted in Fig. 15. The lower wear mass loss in the case of Type 2 and Type 4 heat-treated sample is due to their enhanced hardness. The higher mass loss of Type 1 and Type 3 heat-treated samples attributes to the softness of the

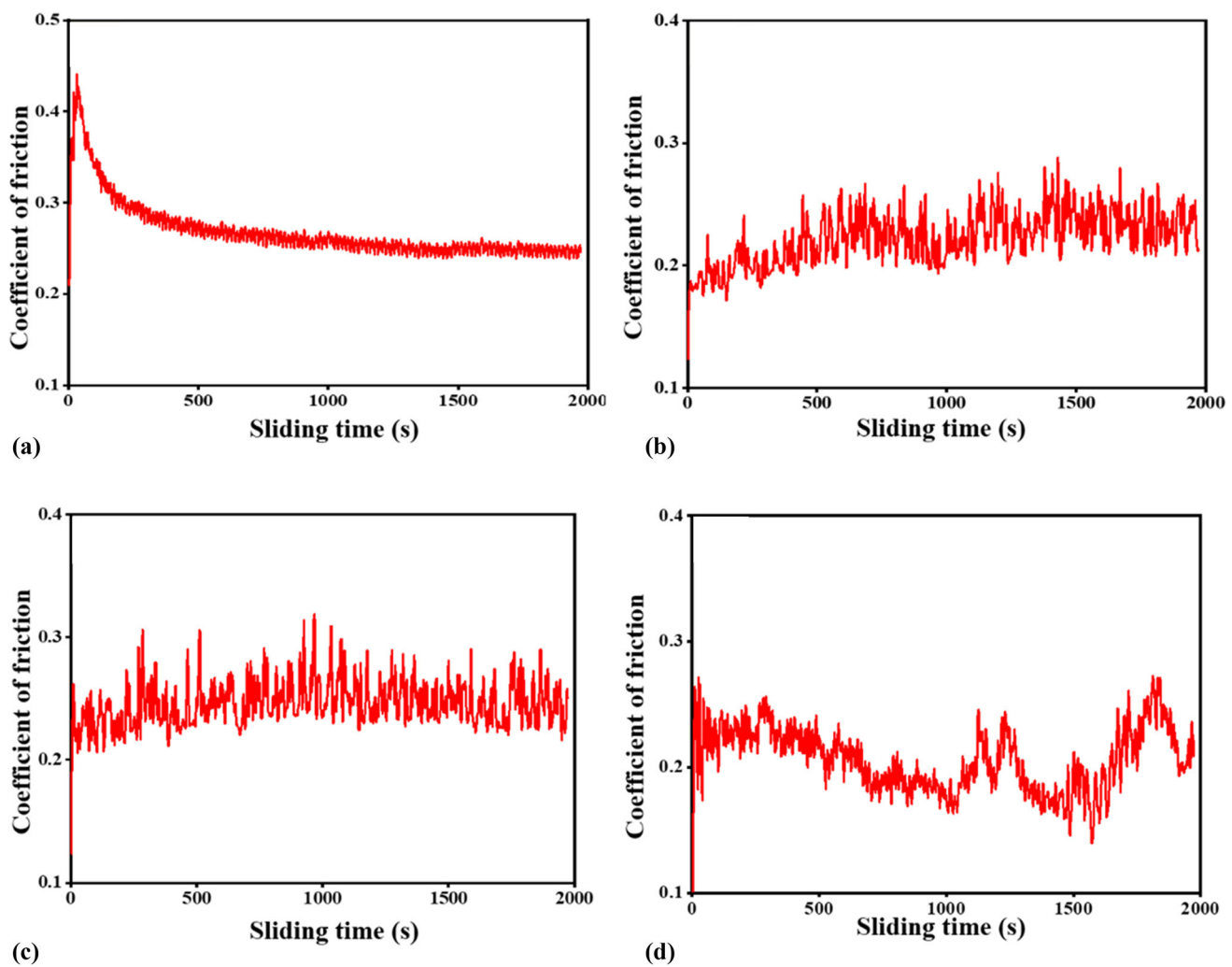


Fig. 13 Coefficient of friction versus sliding time of the cladded (and milled) layer along the cladding direction after different heat treatment procedures: (a) Type 1 (b) Type 2, (c) Type 3 and (d) Type 4

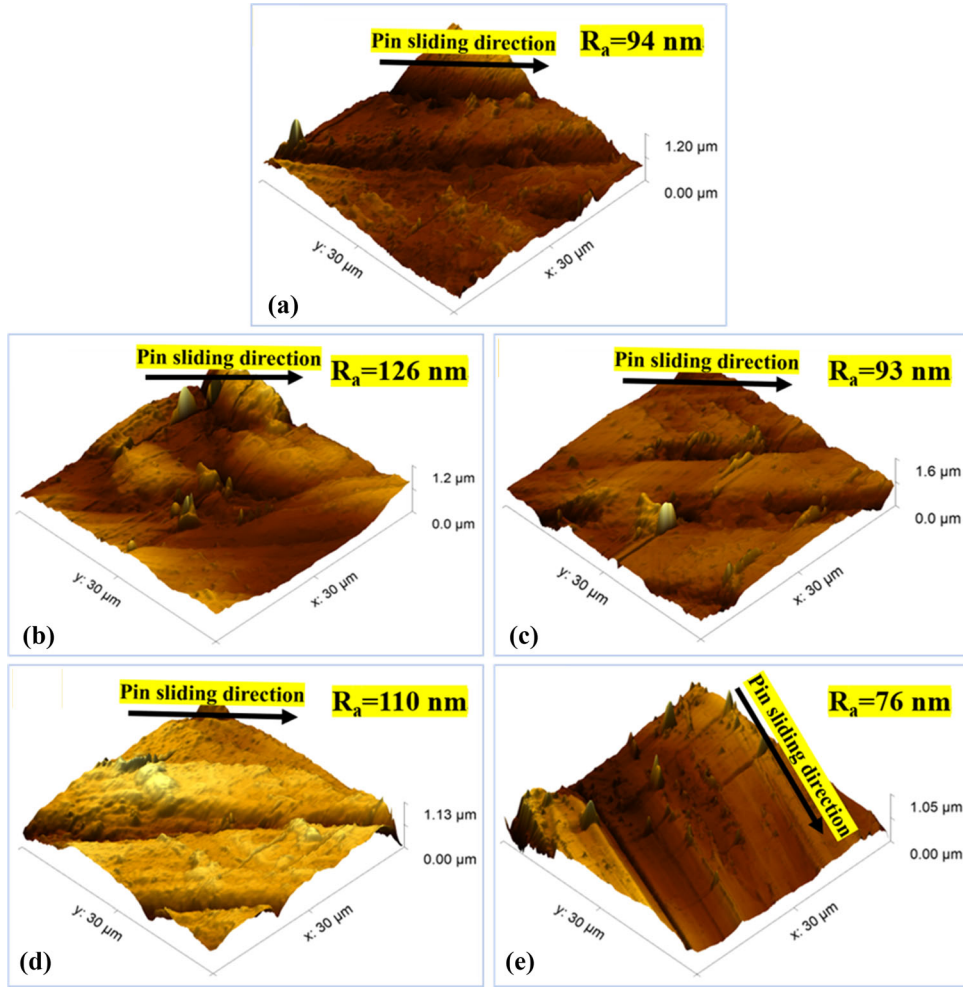


Fig. 14 AFM 3D micrograph of worn-out surface: (a) as-cladded, (b) Type 1, (C) Type 2, (d) Type 3 and (e) Type 4

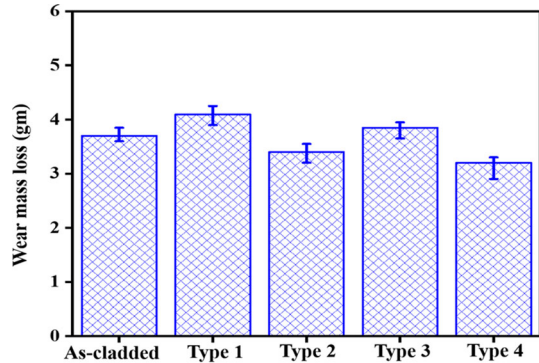


Fig. 15 Wear mass loss of cladded layer due to heat treatment

surface, which caused significant plastic flow during sliding against steel surface. Increased mass loss is a result of increased pin (cladded layer) and disc (hardened steel) contact area. The Type 4 heat-treated samples surface comprises homogeneous and fine distribution of hard martensite and carbide, respectively. The hard debris in the worn surface behaves as an asperity and reduces the true contact between the sample surface and counter body. The reduced grain boundary and hard asperity acted as a strong barrier in material removal during dry-sliding. An oxide layer formed as a result of the microther-

mal action during sliding contact between the pin and disc. This oxide layer acted as a barrier, preventing true metal-to-metal contact.

The mean wear depth values of as-cladded and different heat-treated samples are given in Table 1. The strengthening mechanisms and grain refinement effects due to heat treatment of cladded layer are responsible for reducing the wear depth and wear volume. The XRD analysis indicated that additional dislocations were developed during Type 2 and Type 4 heat treatment. Dislocation mobility gets restricted with increasing dislocation density, thus increasing the hardness. In both adhesive and abrasive wear modes, the hardness is inversely correlated to the wear volume, which is also observed in Table 1. Table 1 shows that the harder is the material, the lesser is the wear volume. The Archard equation for wear (Ref 49) is given as

$$V = K \frac{F_n s}{H}, \quad (\text{Eq 15})$$

where V represents the wear volume, s is the sliding distance, F_n is the applied load, H is the hardness and K is a coefficient. In this case, Archard's law is qualitatively satisfied; although V reduces as hardness increases, the product of VH is not constant for fixed F_n and s . The Lancaster wear coefficient, a measure of severity of the wear, is given as (Ref 50):

Table 1 Wear data of different heat-treated sample

Sample	Hardness, HV	Mean wear depth, μm	Wear volume, $\text{mm}^3 \times 10^{-3}$	Lancaster wear coefficient, $\text{mm}^3/\text{Nm} \times 10^{-5}$
Type 1	+9 181–8	+3 51–4	+0.04 0.50–0.03	+0.07 1.08–0.09
	+6 331–4	+3 34–2	+0.02 0.43–0.01	+0.05 0.93–0.03
Type 2	+5 204–3	+2 42–1	+0.03 0.49–0.02	+0.04 1.06–0.02
	+6 407–7	+2 29–3	+0.02 0.40–0.03	+0.05 0.86–0.07

$$k = \frac{V}{F_n s}. \quad (\text{Eq } 16)$$

The lesser the value of the k , the greater is the wear resistance. Table 1 shows that k is greater for softer material. The Lancaster wear coefficient of as-cladded samples was $1.01 \times 10^{-5} \text{ mm}^3/\text{Nm}$, measured under similar test conditions (Ref 28).

The worn surfaces identified by FESEM are shown in Fig. 16. The morphology is different for different types of heat treatment. Type 1 provides softer surface. Here the wear comprises plowing, spalling and deep grooves. Type 2 (water-quenching) has presence of some cracks. Type 3 morphology is similar to that of Type 1. However, here some delamination is

observed. Type 4 offers the highest wear resistance, showing the absence of deep grooves. The line EDS analysis results at the worn surface of Type 4 heat-treated sample are shown in Fig. 17. The hike in oxygen is marked by arrow in the micrograph. A significant amount of oxidation had occurred during the wear. The Fe oxide could be easily scraped off on the cladded worn surface and transferred as secondary abrasive particles, enhancing abrasive wear during sliding. Furthermore, as a result of the temperature rise from friction heat during dry sliding wear, the contact surface between the cladded surface and the counterpart became relative softer. As a result, there was more debris on the friction surface, which produced more visible micro-cut. The development of worn debris from adhesive wear may encourage three body abrasive wear (Ref 51).

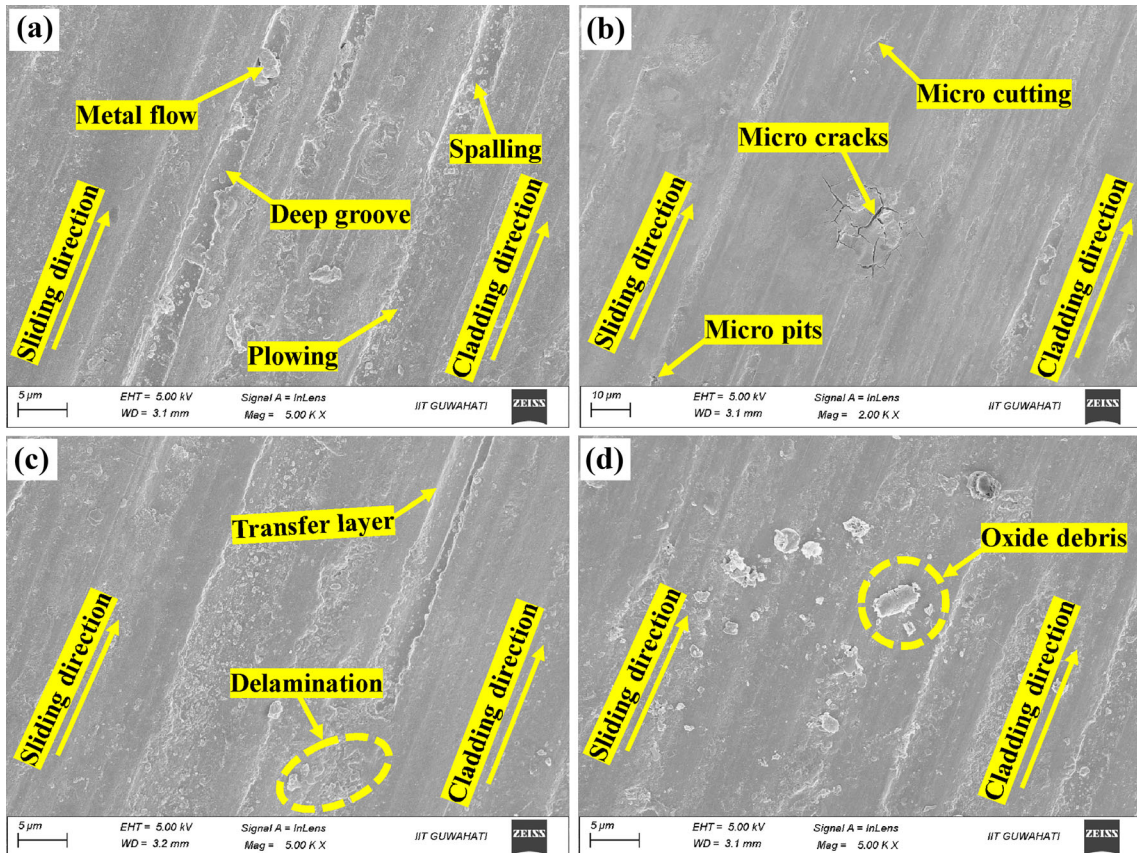


Fig. 16 Worn out surface FESEM morphology of cladded layer: (a) Type 1 (b) Type 2, (c) Type 3 and (d) Type 4

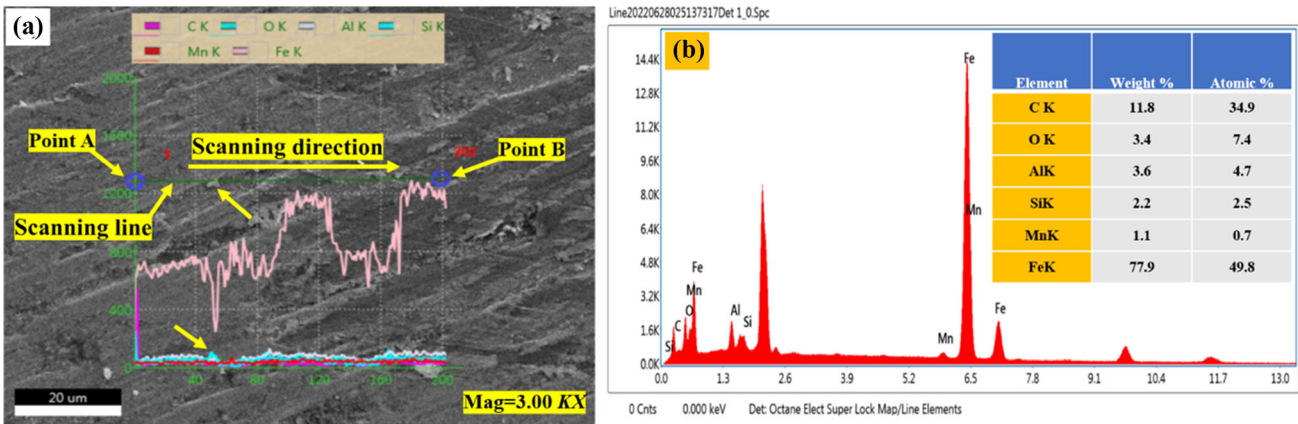


Fig. 17 Line EDS analysis at the worn-out top surface (XY plane; X- and Y-axis as per Fig. 1 and Fig. 4) of Type 4 heat-treated sample: (a) elemental distribution graphs along the scanning line from point A to B and (b) corresponding elemental distribution

3.9 Wear Debris Analysis

The wear debris morphologies of different heat-treated samples are shown in Fig. 18. The irregular shape morphology of the debris in Type 1 heat-treated samples indicates that material was removed by severe sliding and fatigue. During severe sliding, the debris was produced by high adhesive forces and had parallel scratches or grooves on the surface (as seen in the enlarged Fig. 18b). This is mainly because of low surface hardness of Type 1 heat-treated samples. The regular shape morphology of the debris in Type 2 heat-treated samples indicates that material was removed by rubbing and mild adhesion. The debris is smaller in size having smooth surface and edges (Fig. 18c, d). The elongated and curl shape morphology of the debris in Type 3 heat-treated samples indicates that material was removed by cutting and plowing action. Figure 18(e, f) indicates that sharp edges of debris also contributed to cutting and plowing action.

The spherical shape morphology of the debris in Type 4 heat-treated samples indicates that material was removed by sliding, welding and grinding (Fig. 18g, h). The parallel fringes are also observed on the debris-serrated side, indicating the development of shear band (enlarged Fig. 18h). This type of wear mechanism is due to high hardness of Type 4 samples. The analysis of debris morphology can be used for condition monitoring (Ref 52).

3.10 Tensile Property and Fracture Behavior

The mechanical properties are shown in Table 2. The highest yield strength (YS) and ultimate tensile strength (UTS) of 336 MPa and 431 MPa, respectively, were observed in Type 4 heat-treated sample; and the lowest YS and UTS of 232 MPa and 307 MPa, respectively, were observed in Type 1 heat-treated sample. As-cladded (and milled) sample had YS and UTS as 300 MPa and 360 MPa, respectively (Ref 28). The total elongation increased to 16% in Type 1 heat-treated sample and reduced to 9% in Type 4 heat-treated sample compared to as-cladded sample, which was 11% (Ref 28). Increased strength in Type 4 and Type 2 heat-treated samples is mainly due to

Hall-Petch effect. Transformation of soft and ductile austenite to hard and brittle martensite during Type 2 and Type 4 heat treatment also contributed to strength enhancement. It was observed that the dislocation density was higher in case of Type 2 and Type 4 heat-treated sample. This also enhanced the mechanical strength of the cladded layer. The findings of present tensile results match with the findings of Astaf'ev (Ref 53). According to Astaf'ev, the austenite grains in the steel microstructure can be refined to improve the material mechanical properties, including hardness, YS and UTS. The present report also explained that by refining austenite grain size, the YS is also enhanced. It can be justified based on Hall-Petch equation (Ref 44, 45):

$$\sigma_y = \sigma_i + \frac{k_y}{\sqrt{d}} \quad (\text{Eq 17})$$

where k_y is material constants, σ_i is the lattice friction stress, σ_y is the yield stress, and d is the average grain diameter. In order to assess the effectiveness of this relation, constants σ_i and k_y are obtained from the average grain size and YS data of Type 1 and Type 4 heat treatment. Fitting the equation in this matter makes prediction for other cases in interpolation rather than in extrapolation. Hence, substituting the values of d and σ_y in Eq. (17), two simultaneous equations provided, $\sigma_i = -218$ MPa and $k_y = 2476$. With these values, the calculated YS values are 260 MPa, 290 MPa and 243 MPa for as-cladded, Type 2 and Type 3 specimens, respectively. Corresponding measured YS values are 300 MPa, 305 MPa and 251 MPa, which show very good agreement with the calculated values, the maximum deviation being 13.33%. However, it is difficult to justify the negative value of lattice friction stress.

Figure 19 shows the fracture morphology of different heat-treated sample. Figure 19(a-d) shows the fracture surface of cladded portion. Figure 19(e) shows the fracture surface of the substrate portion. The fracture morphology depicts the presence of both brittle and ductile behavior. The ductile section with dimple features and the brittle portion with characteristics of river patterns and rocky surface are visible at the fracture

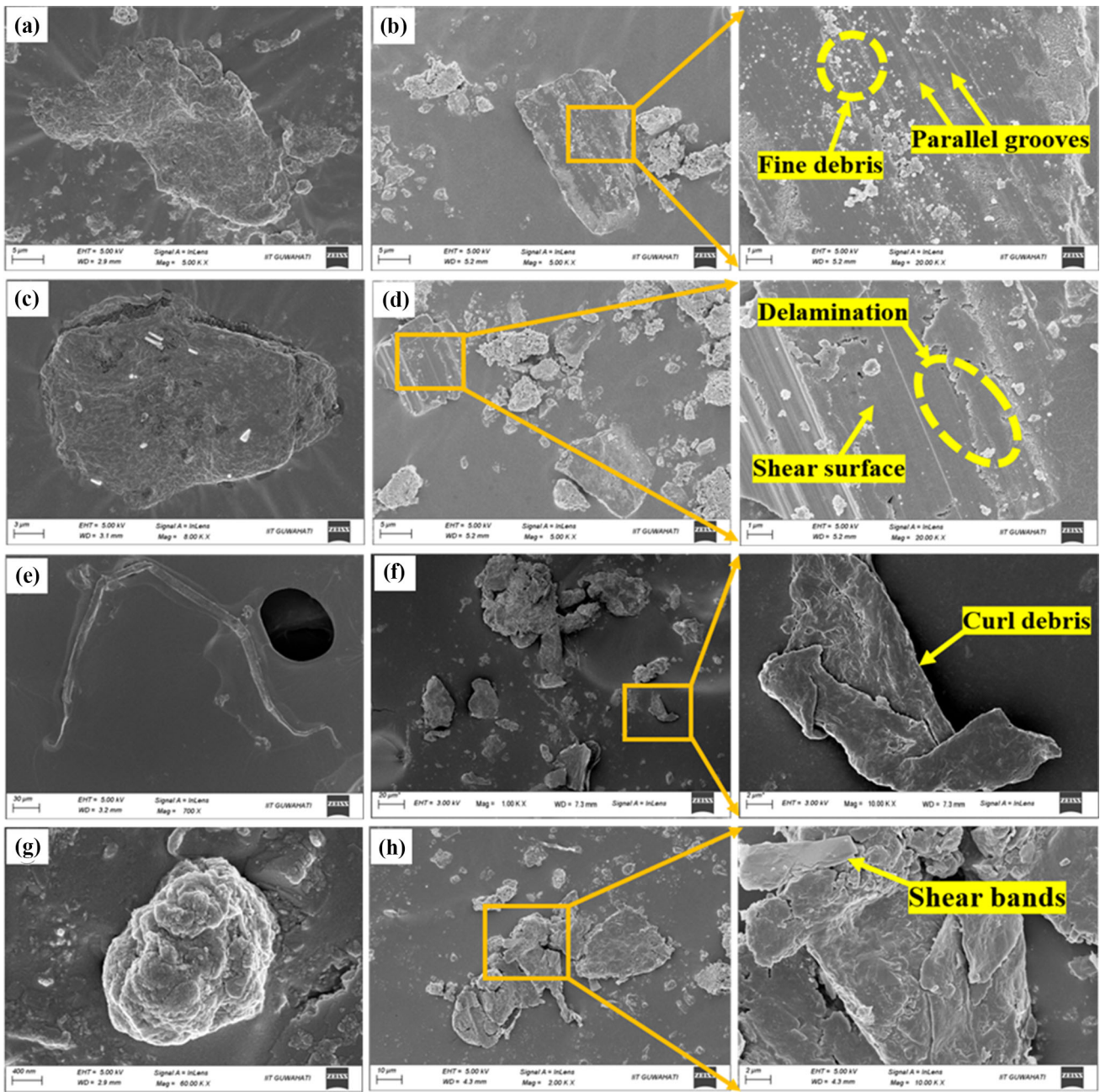


Fig. 18 FESEM morphology of worn-out debris: (a, b) Type 1 (c, d) Type 2, (e, f) Type 3 and (g, h) Type 4

Table 2 Yield strength, ultimate tensile strength and elongation of various samples

Sample	Yield strength, MPa	Ultimate tensile strength, MPa	Elongation, %
Type 1	+6 232–7	+9 307–7	+1 16–2
	+6 305–5	+7 370–6	+2 10–1
Type 2	+5 251–3	+7 329–5	+2 13–1
	+5 336–6	+6 431–7	+1 9–2

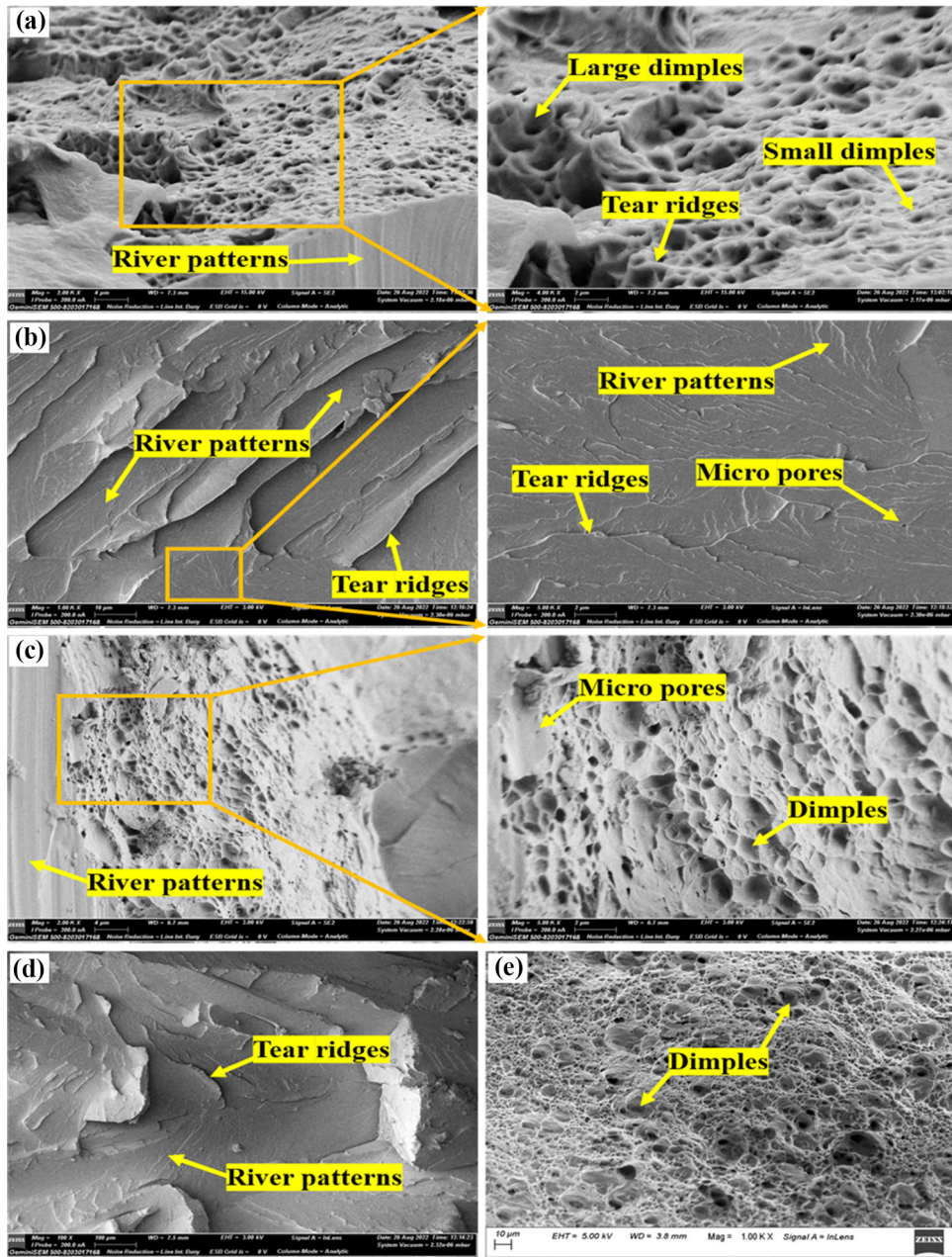


Fig. 19 Fracture FESEM morphology of cladded layer region: (a) Type 1, (b) Type 2, (c) Type 3, (d) Type 4 and (e) substrate region of Type 4

surface. The failure morphology of the Type 1 and Type 3 heat-treated sample comprises mostly mixed ductile–brittle characteristics due to the presence of coarse carbide in the grain boundary and low martensitic phase. The Type 1 and Type 3 heat treatment lead to enhancement of ductility and austenitic phase.

From the fractography of Type 1 and Type 3, it can be seen that the morphology consists of large and deep dimples ($\sim 10 \mu\text{m}$ in diameter) on the major parts, which are typically caused by inclusions and undissolved precipitate phase. Only at small regions between the large dimples, small ($< 1 \mu\text{m}$ in diameter) or secondary dimples are observed. Secondary dimples are formed at the intersection of two major dimples.

The presence of dimples in the Type 1 and Type 3 indicates gradual degradation of mechanical strength. Comparing Type 1 and Type 3, the Type 1 heat-treated sample had large distribution of deep dimples that caused low mechanical strength.

The fractography of Type 2 and Type 4 heat-treated sample comprises mostly brittle features as shown in Fig. 19(b, d), respectively. From the microstructure morphology in Fig. 4, it is observed that Type 2 and Type 4 heat treatment resulted in a great increase of brittle martensitic phase in the microstructure. This resulted in the reduction of plasticity in the austenite phase and enhancement of the brittle fracture.

Table 3 Properties of different samples

Properties	As-cladded	Heat treated			
		Type-1	Type-2	Type-3	Type-4
Porosity, %	2.56	1.35	1.51	1.72	2.08
Martensite phase, %	32	20	43	26	56
Grain size, μm	27	30	24	29	20
Roughness value, nm based on $10 \mu\text{m} \times 10 \mu\text{m}$ area	46	75	41	53	25
Crystallite size, nm	38.94	47.16	32.77	40.77	30.53
Dislocation density, $10^{16}/\text{m}^2$	6.08	4.15	8.47	5.67	10.78
Hardness, HV	237	181	331	204	407
Coefficient of friction	0.23	0.26	0.22	0.24	0.20
Lancaster wear coefficient, mm^3/Nm	1.01	1.08	0.93	1.06	0.86
Yield strength, MPa	300	232	305	251	336
UTS, MPa	360	307	370	329	431
Percentage elongation	11	16	10	13	9
Fracture behavior	Mostly brittle	Both ductile and brittle	Mostly brittle	Both ductile and brittle	Mostly brittle

4. Comparison of Four Heat Treatment Methods

Four different types of heat treatment methods, i.e., Type 1: furnace cooling, Type 2: water quenching, Type 3: artificial age hardening and Type 4: deep cryo-treatment, are compared in Table 3. It is clear that Type 4 heat treatment could make the maximum enhancement in the mechanical properties thanks to grain refinement and diffusion-less transformation to martensite. However, it causes some reduction in ductility. Next best treatment for the enhancement of mechanical properties is Type 2 heat treatment. Type 1 heat treatment also enhances the ductility but defeats the very purpose of cladding by weakening the tribological properties.

5. Conclusions

In this work, various types of heat treatments were carried out on steel cladded aluminum alloy samples. Cladding was carried out with CMT technology. Four different types of heat treatment were carried out. Microstructural, tribological and mechanical characteristics were examined. The following are the salient observations:

- The porosity in the cladded samples decreased to approximately 0.48-1.21% after heat treatment process. The type of heat treatment and temperature significantly affects in the grain size. The average grain size increased to $30 \mu\text{m}$ after Type 1 heat treatment, compared to $27 \mu\text{m}$ in the as-cladded layer. However, during Type 4 heat treatment the average grain size reduced to $20 \mu\text{m}$. Grain size is positively correlated with the yield and tensile strength.
- The minimum surface roughness was obtained in Type 4 heat-treated sample (cryogenic treatment) due to the grain refinement and absence of oxidation. The martensite transformation was also observed to be high during Type 4 heat treatment with fine and homogeneous carbide precipitates at the grain.
- The maximum dislocation density of $10.78 \times 10^{16}/\text{m}^2$ was observed in case of Type 4 heat treatment, while the

minimum was of $4.15 \times 10^{16}/\text{m}^2$ in the Type 1 heat treatment compared to $6.08 \times 10^{16}/\text{m}^2$ in the as-cladded layer.

- In terms of mechanical properties also, Type 4 heat treatment stands the best. The grain refinement, dense martensitic phase and enhanced dislocation density have resulted in enhanced hardness of 407 HV. Lancaster wear coefficient of $0.86 \times 10^{-5} \text{ mm}^3/\text{Nm}$ and tensile strength 336 MPa were observed in Type 4 heat treatment.

Thus, overall cryogenic treatment of steel cladded parts produced through CMT technology enhanced the properties of the cladded layer in a significant manner. The second best heat treatment was water quenching (Type 2). Furnace cooling enhanced the ductility but had an adverse effect on the tribological properties.

Acknowledgments

The Central Instrumentation Facility of the Indian Institute of Guwahati (IITG) provided the testing facility and CMT Welding Machine used in this work was procured by IITG Technology Innovation and Development Foundation, which has been set up at IIT Guwahati as a part of the National Mission on Interdisciplinary Cyber Physical Systems (NMICPS) through grant number DST/NMICPS/TIH12/IITG/2020. The authors also acknowledge North East Centre for Biological Sciences and Healthcare Engineering, IITG, and Department of Biotechnology, Govt. of India, for FESEM facility under Project No. BT/COE/34/SP28408/2018. Assistance of Mr. Abhijeet Dhulekar in conducting experiments is gratefully acknowledged.

References

- S. Selvi, A. Vishvaksenan, and E. Rajasekar, Cold Metal Transfer (CMT) Technology—An Overview, *Def. Technol.*, 2018, **14**(1), p 28–44. <https://doi.org/10.1016/j.dt.2017.08.002>
- C.G. Pickin, S.W. Williams, and M. Lunt, Characterization of the Cold Metal Transfer (CMT) Process and Its Application for Low Dilution Cladding, *J. Mater. Proc. Technol.*, 2011, **211**, p 496. <https://doi.org/10.1016/j.jmatprotec.2010.11.005>

3. G.P. Rajeev, M. Kamaraj, and R.S. Bakshi, Comparison of Microstructure, Dilution and Wear Behavior of Stellite 21 Hardfacing on H13 Steel Using Cold Metal Transfer and Plasma Transferred Arc Welding Processes, *Surf. Coating. Technol.*, 2019, **375**, p 383–394. <https://doi.org/10.1016/j.surfcoat.2019.07.019>
4. G.P. Rajeev, M. Kamaraj, and R.S. Bakshi, Hardfacing of AISI H13 Tool Steel with Stellite 21 Alloy Using Cold Metal Transfer Welding Process, *Surf. Coat. Technol.*, 2017, **326**, p 63–71. <https://doi.org/10.1016/j.surfcoat.2017.07.050>
5. T.B. Thiagarajan and S. Ponnusamy, Effect of Cladding of Stellite-6 Filler Wire on the Surface of ss316l Alloy Through Cold Metal Arc Transfer Process, *J. Met. Mater. Miner.*, 2021, **31**(3), p 70–84.
6. P. Varghese, E. Vetrivendan, M.K. Dash, S. Ningshen, M. Kamaraj, and U.K. Mudali, Weld Overlay Coating of Inconel 617M on Type 316 L Stainless Steel by Cold Metal Transfer Process, *Surf. Coat. Technol.*, 2019, **357**, p 1004–1013. <https://doi.org/10.1016/j.surfcoat.2018.10.73>
7. A. Evangeline and P. Sathiya, Cold Metal Arc Transfer (CMT) Metal Deposition of Inconel 625 Superalloy on 316L austenitic Stainless Steel: Microstructural Evaluation, Corrosion and Wear Resistance Properties, *Mater. Res. Express.*, 2019, **6**, p 066516. <https://doi.org/10.1088/2053-1591/ab0a10>
8. O.T. Ola and F.E. Doern, A Study of Cold Metal Transfer Clads in Nickel-Base INCONEL 718 Superalloy, *Mater. Des.*, 2014, **57**, p 51–59. <https://doi.org/10.1016/j.matdes.2013.12.060>
9. H. Kun, D. Lijin, W. Qinying, Z. Huali, L. Yufei, L. Li, and Z. Zhi, Comparison on the Microstructure and Corrosion Behavior of Inconel 625 Cladding Deposited by Tungsten Inert Gas and Cold Metal Transfer Process, *Surf. Coating. Technol.*, 2022, **435**, p 128245. <http://doi.org/10.1016/j.surfcoat.2022>
10. S. Monika, K. Agnieszka, R. Agnieszka, and R. Bogdan, Microstructure, Microsegregation and Nanohardness of CMT Clad Layers of Ni-base Alloy on 16Mo3 Steel, *J. Alloy. Compd.*, 2018, **751**, p 86–95. <https://doi.org/10.1016/j.jallcom.2018>
11. X. Tang, S. Zhang, X. Cui, C. Zhang, Y. Liu, and J. Zhang, Tribological and Cavitation Erosion Behaviors of Nickel-Based and Iron-Based Coatings Deposited on AISI 304 Stainless Steel by Cold Metal Transfer, *J. Mater. Res. Technol.*, 2020, **9**, p 6665–6681. <https://doi.org/10.1016/j.jmrt.2020.04.064>
12. G.P. Rajeev, M. Kamaraj, and R.S. Bakshi, Al-Si-Mn Alloy Coating on Aluminum Substrate Using Cold Metal Transfer (CMT) Welding Technique, *JOM*, 2014, **66**, p 1061–1067. <https://doi.org/10.1007/s11837-014-0970-7>
13. Z. Bowen, W. Chao, W. Zhaohui, Z. Laiqi, and G. Qiang, Microstructure and Properties of Al Alloy ER5183 Deposited by variable Polarity Cold Metal Transfer, *J. Mater. Process. Technol.*, 2019, **267**, p 167–176. <https://doi.org/10.1016/j.jmatprotec.2018.12.011>
14. P. Luchtenberg, P.T. Campos, P. Soares, C.A.H. Laurindo, O. Maranho, and R.D. Torres, Effect of Welding Energy on the Corrosion and tribological Properties of Duplex Stainless-Steel Weld Overlay Deposited by GMAW/CMT Process, *Surf. Coat. Technol.*, 2019, **375**, p 688–693. <https://doi.org/10.1016/j.surfcoat.2019.07.072>
15. W.Y. Li, C.J. Li, and H. Liao, Effect of Annealing Treatment on the Microstructure and Properties of Cold-Sprayed Cu Coating, *J. Therm. Spray Technol.*, 2006, **15**, p 206–211. <https://doi.org/10.1361/105996306X108066>
16. F. Gärtner, T. Stoltenhoff, J. Voyer, H. Kreye, S. Riekehr, and M. Koçak, Mechanical Properties of Cold-Sprayed and thermally Sprayed Copper Coatings, *Surf. Coat. Technol.*, 2006, **200**(24), p 6770–6782. <https://doi.org/10.1016/j.surfcoat.2005>
17. V. Luzin, K. Spencer, and M.-X. Zhang, Residual Stress and Thermo-Mechanical Properties of Cold Spray Metal Coatings, *Acta Mater.*, 2011, **59**(3), p 1259–1270. <https://doi.org/10.1016/j.actamat.2010>
18. R. Ghelichi, S. Bagherifard, D. MacDonald, I. Fernandez-Pariente, B. Jodoin, and M. Guagliano, Experimental and Numerical Study of Residual Stress Evolution in Cold Spray Coating, *Appl. Surf. Sci.*, 2014, **288**, p 26–33. <https://doi.org/10.1016/j.apsusc.2013>
19. S. Prakash, R. John Felix Kumar, and S. Jerome, Effect of Heat Treatment on Microstructure and Mechanical Properties of CMT WELDED ALUMINUM ALLOY 2024, *Mater. Today Proc.*, 2018, **5**(13), p 26997–27003. <https://doi.org/10.1016/j.mtpr.2018>
20. R. Ahmad and M.A. Bakar, Effect of a Post-Weld Heat Treatment on the Mechanical and Microstructure Properties of AA6061 Joints Welded by the Gas Metal Arc Welding Cold Metal Transfer Method, *Mater. Des.*, 2011, **32**(10), p 5120–5126. <https://doi.org/10.1016/j.matedes.2011>
21. Y. Shanglu, Z. Jing, L. Jin, and L. Yongpin, Welding of Aluminum Alloy to Zinc Coated Steel by Cold Metal Transfer, *Mater. Des.*, 2013, **2013**(49), p 602–612. <https://doi.org/10.1016/j.matedes.2013>
22. P. Sudharshan, R.D. Srinivasa, S.V. Joshi, and G. Sundararajan, Effect of Process Parameters and Heat Treatments on Properties of Cold Sprayed Copper Coatings, *J. Therm. Spray Technol.*, 2007, **16**, p 425–434. <https://doi.org/10.1007/s11666-007-9048-1>
23. B. Hengyong, Y. Mohammed, L. Chen, and J. Bertrand, Effect of Heat Treatment on the Intermetallic Layer of Cold Sprayed Aluminum Coatings on Magnesium Alloy, *Surf. Coat. Technol.*, 2011, **205**(19), p 4665–4671. <https://doi.org/10.1016/j.surfcoat.2011.04.018>
24. M. Xian-Ming, Z. Jun-Bao, H. Wei, Z. Jie, and L. Yong-Li, Influence of Annealing Treatment on the Microstructure and Mechanical Performance of Cold Sprayed 304 Stainless Steel Coating, *Appl. Surf. Sci.*, 2011, **258**(2), p 700–704. <https://doi.org/10.1016/j.apsusc.2011.07.107>
25. B. Al-Mangour, V. Phuong, M. Rosaire, I. Eric, and Y. Stephen, Effect of Heat Treatment on the Microstructure and Mechanical Properties of Stainless Steel 316L Coatings Produced by Cold Spray for Biomedical Applications, *J. Therm. Spray Technol.*, 2014, **23**, p 641–652. <https://doi.org/10.1007/s11666-013-0053-2>
26. R.M. Molak, H. Araki, M. Watanabe, H. Katanoda, N. Ohno, and S. Kuroda, Effects of Spray Parameters and Post-spray Heat Treatment on Microstructure and Mechanical Properties of Warm-Sprayed Ti-6Al-4V Coatings, *J. Therm. Spray Technol.*, 2017, **26**, p 627–647. <https://doi.org/10.1007/s11666-016-0494-5>
27. W. Wong, E. Irisou, P. Vo, M. Sone, F. Bernier, J.G. Legoux, H. Fukanuma, and S. Yue, Cold Spray Forming of Inconel 718, *J. Therm. Spray Technol.*, 2013, **22**, p 413–421. <https://doi.org/10.1007/s11666-012-9827-1>
28. B. Das, B.N. Panda, and U.S. Dixit, Microstructure and Mechanical Properties of ER70S-6 Alloy Cladding on Aluminum Using a Cold Metal Transfer Process, *J. Mater. Eng. Perform.*, 2022 <https://doi.org/10.1007/s11665-022-06937-8>
29. T. Ponomareva, M. Ponomarev, A. Kisarev, and M. Ivanov, Wire Arc Additive Manufacturing of Al-Mg Alloy with the Addition of Scandium and Zirconium, *Materials*, 2021, **14**, p 3665. <https://doi.org/10.3390/ma14133665>
30. <https://www.malvernpanalytical.com/en/products/category/software/x-ray-diffraction-software/highscore-with-plus-option>, Accessed on January 29, 2023
31. F. Bin-you, H. Ding-yong, and Z. Li-dong, Effect of Heat Treatment on the Microstructure and Mechanical Properties of Fe-Based Amorphous Coatings, *J. Alloy. Compd.*, 2009, **480**(2), p 422–427. <https://doi.org/10.1016/j.jallcom.2009.02.107>
32. S. Harish, A. Bensely, D.M. Lal, A. Rajadurai, and G.B. Lenkey, Microstructural Study of Cryogenically Treated En 31 Bearing Steel, *J. Mater. Process. Technol.*, 2009, **209**(7), p 3351–3357. <https://doi.org/10.1016/j.jmatprotec.2008.07.046>
33. R.C. Chen, C. Hong, J.J. Li, Z.Z. Zheng, and P.C. Li, Austenite Grain Growth and Grain Size Distribution in Isothermal Heat-Treatment of 300M Steel, *Procedia Eng.*, 2017, **207**, p 663–668. <https://doi.org/10.1016/j.proeng.2017.10.1038>
34. L.H. Manjunatha, M. Lokesh, and B. Ajaykumar, A review: Mechanical Properties of HSS Steel by deep Cryo-Treatment, *IOP Conf. Ser. Mater. Sci. Eng.*, 2018, **376**, p 012098. <https://doi.org/10.1088/1757-899X/376/1/012098>
35. L. Yuhua, C. Yongli, and Z. Xuejiao, Effects of Cryogenic Treatment and Tempering on Mechanical Properties and Microstructure of 0.25C–0.80Si-1.6Mn Steel, *Adv. Mater. Sci. Eng.*, 2020 <https://doi.org/10.1155/2020/1501474>
36. C. Wen-Ruey, H. Mikko, and G. Raoul, The Effects of Cut-Off Length on Surface Roughness Parameters and Their Correlation with Transition Friction, *Saf. Sci.*, 2004, **42**, p 755–769. <https://doi.org/10.1016/j.ssci.2004.01.002>
37. R. Jenkins and R.L. Snyder, *Introduction to X-Ray Powder Diffraction*, J Wiley & Sons Inc, New York, 1996
38. S. Joydip, R.K. Sahoo, K.K. Bardhan, and C.D. Mukherjee, Influence of Annealing Temperature on the Structural, Topographical and Optical Properties of Sol-Gel Derived ZnO Thin Films, *Mater. Lett.*, 2011, **65**, p 2572–2574. <https://doi.org/10.1016/j.matlet.2011.06.021>

39. A.M. Rashidi and A. Amadeh, The Effect of Saccharin Addition and Bath Temperature on the Grain Size of Nanocrystalline Nickel Coatings, *Surf. Coating. Technol.*, 2009, **204**(3), p 353–358. <https://doi.org/10.1016/j.surcoat.2009.07.036>
40. J.Y. He, H. Wang, H.L. Huang, X.D. Xu, M.W. Chen, Y. Wu, X.J. Liu, T.G. Nieh, K. An, and Z.P. Lu, A Precipitation-Hardened high-Entropy Alloy with Outstanding Tensile Properties, *Acta Mater.*, 2016, **102**, p 187–196. <https://doi.org/10.1016/j.actamat.2015.08.076>
41. Y.H. Zhao, H.W. Sheng, and K. Lu, Microstructure Evolution and Thermal Properties in Nanocrystalline Fe During Mechanical Attrition, *Acta Mater.*, 2001, **49**(2), p 365–375. [https://doi.org/10.1016/S1359-6454\(00\)00310-4](https://doi.org/10.1016/S1359-6454(00)00310-4)
42. J.Y. Huang, Y.T. Zhu, X.Z. Liao, I.J. Beyerlein, M.A. Bourke, and T.E. Mitchell, Microstructure of Cryogenic Treated M2 Tool Steel, *Mater. Sci. Eng. A*, 2003, **339**, p 241–244. [https://doi.org/10.1016/S0921-5093\(02\)00165-X](https://doi.org/10.1016/S0921-5093(02)00165-X)
43. S.H.M. Anijdan, M. Sabzi, M. Ghoberti-Hasab, and A. Roshan-Ghiyas, Optimization of Spot-Welding Process Parameters in Dissimilar Joint of Dual Phase Steel DP600 and AISI 304 Stainless Steel to Achieve the Highest Level of Shear-Tensile Strength, *Mater. Sci. Eng. A*, 2018, **726**, p 120–125. <https://doi.org/10.1016/j.msea.2018.04.072>
44. E.O. Hall, *Proc. Phys. Soc. Series B*, 1951, **64**, p 747.
45. N.J. Petch, *Proc. Swampscott Conf.* MIT Press, 1955, 54
46. D. Das, A.K. Dutta, V. Toppo, and K.K. Ray, Effect of Deep Cryogenic Treatment on the Carbide Precipitation and Tribological Behavior of D2 Steel, *Mater. Manuf. Process.*, 2007, **22**, p 474–480. <https://doi.org/10.1080/10426910701235934>
47. J. Denape and J. Lamon, Sliding Friction of Ceramics: Mechanical Action of the Wear Debris, *J. Mater. Sci.*, 1990, **25**, p 3592–3604. <https://doi.org/10.1007/BF00575394>
48. H.Q. Sun, Y.N. Shi, and M.X. Zhang, Wear Behaviour of AZ91D Magnesium Alloy with a Nanocrystalline Surface Layer, *Surf. Coat. Technol.*, 2008, **202**(13), p 2859–2864. <https://doi.org/10.1016/j.surcoat.2007.10.025>
49. J. Archard, Contact and Rubbing of Flat Surfaces, *J. Appl. Phys.*, 1953, **24**, p 981–988. <https://doi.org/10.1063/1.1721448>
50. J.K. Lancaster, The Influence of Substrate Hardness on the Formation and Endurance of Molybdenum Disulphide Films, *Wear*, 1967, **10**, p 103–117. [https://doi.org/10.1016/0043-1648\(67\)90082-8](https://doi.org/10.1016/0043-1648(67)90082-8)
51. M. Qunshuang, L. Yajiang, W. Juan, and L. Kun, Microstructure Evolution and Growth Control of Ceramic Particles in Wide-Band Laser Clad Ni60/WC Composite Coatings, *Mater. Des.*, 2016, **92**(15), p 897–905. <https://doi.org/10.1016/j.matdes.2015.12.121>
52. Z. Peng and T.B. Kirk, Computer Image Analysis of Wear Particles in Three-Dimensions for Machine Condition Monitoring, *Wear*, 1998, **223**, p 157–166. [https://doi.org/10.1016/S0043-1648\(98\)00280-4](https://doi.org/10.1016/S0043-1648(98)00280-4)
53. A.A. Astaf'ev, Effect of Grain Size on the Properties of Manganese Austenite Steel 110G13L, *Met. Sci. Heat Treat.*, 1997, **39**, p 198–201. <https://doi.org/10.1007/BF02467284>

Publisher's Note Springer Nature remains neutral with regard to jurisdictional claims in published maps and institutional affiliations.

Springer Nature or its licensor (e.g. a society or other partner) holds exclusive rights to this article under a publishing agreement with the author(s) or other rightsholder(s); author self-archiving of the accepted manuscript version of this article is solely governed by the terms of such publishing agreement and applicable law.